

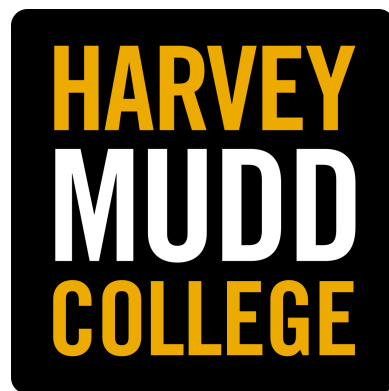


Modulating the Stability Boundary: Secular Dynamics of Compact Three-planet Systems

Eritas Yang

Daniel Tamayo, Advisor

May, 2024



Department of Physics

Copyright © 2024 Eritas Yang.

The author grants Harvey Mudd College the nonexclusive right to make this work available for noncommercial, educational purposes, provided that this copyright statement appears on the reproduced materials and notice is given that the copying is by permission of the author. To disseminate otherwise or to republish requires written permission from the author.

Abstract

The final stage in terrestrial planet formation occurs after the gas disk, out of which planets accrete, dissipates and removes its stabilizing effects. This giant impact phase, characterized by violent planetary collisions and gravitational scatterings, determines the masses and orbital architectures of planets that we see today. However, the chaotic dynamics driving these instabilities are poorly understood, and elucidating them is crucial for connecting disk formation models to current observations.

It has long been known that the chaotic boundary for a pair of planets on closely spaced orbits is determined by the influence of resonances between their orbital periods. However, the theoretical picture becomes unclear when introducing even one additional planet, while systems with three or more planets are the norm in the observed sample of planetary systems. Three decades of running suites numerical integrations across the parameter space of orbital configurations and fitting empirical scaling laws have shown that instabilities occur over a much broader range of parameters in multiplanet systems. However, the large number of system parameters that sensitively affect stability has limited the applicability of these empirical models.

Recent work suggests that instabilities in multiplanet systems are determined through the same mechanism as in the two-planet case, but one additionally has to account for longer timescale oscillations in the strengths of the implicated resonances. This previous work predicted the stability boundary numerically, but without analytical closed-form expressions, it is impossible to identify the dominant combinations of masses, orbital eccentricities and separations that determine stability, and thus to effectively visualize and sample the high-dimensional parameter space.

In this thesis, we develop an analytical model for the long-term dynamics of coplanar three-planet systems, in the limit where the orbits are closely spaced. This model provides not only analytical expressions but also geometric intuition into the conserved modes driving the dynamics. We then use these results to obtain a closed-form expression for the resulting stability boundary and demonstrate its agreement with a suite of numerical integrations.

Contents

1	Introduction	4
1.1	Motivation	4
1.2	Chaos	5
1.3	Stability in the Three-body Problem	7
1.4	Extending to Multiplanet Systems	9
1.4.1	Numerical Work	9
1.4.2	Analytical Work	9
1.5	Outline	11
2	Two-body MMRs	12
2.1	The Physics of Resonance	12
2.2	The Chaotic Boundary	16
2.3	Generalizing to Two Eccentric Orbits	18
3	Secular Dynamics	20
3.1	Overview	20
3.2	Hamiltonian Laplace-Lagrange Formalism	22
3.3	Compact Two-planet Systems	23
3.4	Compact Three-planet Systems	25
3.4.1	Low-mass Limit	25
3.4.2	Generalization to Wider Spacings	31
3.4.3	Generalization to Massive Middle Planets	31
3.4.4	An Application	34
3.4.5	Summary	36
4	Modulation of the Stability Boundary	37
5	Conclusion	41
A	Three-body MMRs	45
B	Laplace-Lagrange Hamiltonian	48
C	Approximated Eigenvalues	50
D	Extremizing the Secular Modulation	52

List of Figures

1.1	Structure of resonances and their overlap for an eccentric test particle perturbed by a planet on an exterior circular orbit.	8
1.2	Stability times of multiplanet systems as a function of initial spacings.	10
1.3	The evolution of the MMR widths over the secular timescale.	11
2.1	Stable configuration for the test particle and the planet in a 2:1 resonance.	13
2.2	Unstable configuration for the test particle and the planet in a 2:1 resonance.	13
2.3	Schematic diagram of resonant encounters between an eccentric test particle and a planet on an exterior circular orbit.	14
2.4	Phase space plot of a two-planet system described by the pendulum model.	15
2.5	Perturbations from nearby MMRs create layers of chaotic zones around the separatrices. The widths of the layers increase with the test particle's eccentricity.	16
2.6	The MMR overlap criterion predicts the widespread chaos in a system of a test particle subject to an exterior circular perturber.	17
2.7	Schematic illustration of the eccentricity vectors. The relative eccentricity vector determines the orbital geometry and thus the dynamics between the test particle and the planet.	19
3.1	In a compact two-planet system, the eccentricities e_1 and e_2 can be decomposed as the vector sum of contributions from the two Laplace-Lagrange eigenmodes e_{com} and e_{12}	25
3.2	The values of $\tilde{\chi}_{12}$ and $\tilde{\chi}_{23}$ as a function of the mass distribution parameter μ and the spacing asymmetry parameter η . These two parameters describe how strongly the inner pair and the outer pair are interacting respectively.	29
3.3	Analogous plot to Fig. 3.1, for a compact three-planet system where the middle planet is massless.	30

3.4	Error for our compact approximation of the e_- eigenmode, considering an equally spaced ($\eta = 0$) three-planet system with a massless middle planet.	31
3.5	Error for our low-mass approximation of the e_- eigenmode as we increase the mass of the middle planet from the test-particle case to the equal-mass case.	32
3.6	Error in the e_- eigenmode due both to wider spacings and a massive middle planet.	33
3.7	We compare our expressions for the eigenmodes directly against N-body integration, considering a pair of Earth-mass planets with period ratio 1.54 wide of the 3:2 MMR, with a test particle placed approximately in the middle ($\eta = -0.12$).	35
4.1	The stability boundary as we minimize and maximize the secular variations in the relative eccentricities.	40
A.1	Phase space plots of a three-planet system modeled described by the perturbed pendulum model for different values of v	46
A.2	Double surface of section that shows the extent of chaotic regions across different values of v	46
A.3	Chaotic regions due to overlap of two-body MMRs from each pair. .	47
C.1	The value of $\delta \equiv (b_{3/2}^{(1)}(\alpha) - b_{3/2}^{(2)}(\alpha)) / b_{3/2}^{(1)}(\alpha)$ as a function of α	51
D.1	The evolution of each normalized relative eccentricity ($\tilde{e}_{ij} \equiv e_{ij} / e_{c,ij}$) as we minimize and maximize the secular variations of e_{12}	54

Chapter 1

Introduction

1.1 Motivation

When gas collapses in interstellar clouds to form stars, angular momentum conservation spreads part of that material outward into a disk of gas and dust in orbit around the star. In the current planet formation paradigm, dust in this disk coagulates and through various processes can eventually grow to form planets (Armitage, 2018). Detailed analytical and numerical models have been developed to understand this protoplanetary disk phase, which is observationally constrained to last a few Myr (Ribas et al., 2015). However, the observed exoplanet systems, which these models would be compared against, are much older, typically several Gyr, and a lot can happen during this extended period.

In fact, the dissipation of the protoplanetary disk is expected to trigger a series of violent planetary collisions. Gravitational interactions between protoplanets and their natal disk tend to damp any deviations from circular coplanar orbits (Lee & Peale, 2002). Removal of this powerful stabilizing influence on the system is thus thought to set off the final stage of planet formation, called the giant impact phase, where planetary mergers and gravitational scatterings determine the ultimate planetary masses and orbits that we observe at the present day (Goldreich et al., 2004). However, despite extensive effort, the chaotic dynamics driving these instabilities remain poorly understood. A powerful motivation for elucidating the dynamical mechanisms behind such instabilities is therefore to better understand and model how the exoplanet sample has evolved with time.

A second important application is to help constrain the masses and orbits of planets in newly discovered systems, which are often significantly uncertain due to the difficulty of detecting planets around distant stars. Particularly in planetary systems with closely spaced orbits, there are wide swaths of parameter space that would rapidly lead to collisions. This allows one to make a statistical argument (e.g., Gott III, 1993). Stars and new planetary systems have been forming roughly uniformly in time over the Milky Way's history, so when we discover a

random system today, we can imagine ourselves as catching it at a random point in its lifetime. If the system is several Gyr old (estimated by modeling the host star), it should be statistically unlikely that it would destabilize in, e.g., the next Myr – it would imply we were lucky enough to catch it in the last 0.1% of its lifetime, right before its final cataclysm. One can therefore use stability to filter out the dynamically viable subset of orbital parameters that are allowed observationally. Tamayo et al. (2021a) call this approach “stability constrained characterization”, and in planetary systems with close orbits (where many possible orbital configurations are unstable) it provides a powerful theoretical complement to observations yielding much sharper planetary masses and orbital parameters (e.g., Quarles et al., 2017; Tamayo et al., 2017; Lammers & Winn, 2024).

Of course one can always simply check the stability of a given orbital configuration by brute-force numerical integration. Indeed, specialized “N-body” numerical methods have been developed to efficiently and accurately integrate the motions of planetary systems (e.g., Wisdom & Holman, 1991; Chambers, 1999; Rein & Tamayo, 2015). These have been applied both to modeling the giant impact phase (Hansen & Murray, 2012; Dawson et al., 2016) and to stability constrained characterization of particularly important discoveries (Quarles et al., 2017; Wang et al., 2018). However, the Gyr lifetimes of planetary systems and the large parameter space of candidate orbital configurations present a major computational bottleneck for N-body methods and have severely limited the scope of such studies. Machine learning methods have recently been developed to speed up this process by several orders of magnitude (Tamayo et al., 2020; Cranmer et al., 2021), but until we develop an analytical understanding of the dynamics driving these instabilities, we will continue blindly and inefficiently wandering the high-dimensional parameter space of initial conditions that is intrinsic to these important problems.

The overarching aim of this thesis is thus to elucidate the physical processes driving chaos and instabilities in forming planetary systems.

1.2 Chaos

While Isaac Newton solved the two-body problem shortly after formulating his laws of motion and gravity, introducing even one additional planet to the system has defied analytical solution ever since. Early attempts assumed that since the gravitational potential between two planets just depends on their separation and is therefore periodic along the unperturbed two-body orbits (i.e., it remains unchanged if all orbital angles cycle by 2π), one could decompose the solution into a sum of periodic functions, known as a quasi-periodic solution. Laplace and Lagrange were the first to approximate such a solution by expanding the gravitational potential between planets to leading order in orbital eccentricities and inclinations, which are small in our Solar System. This results in a system of

linearly coupled harmonic oscillators that yields quasi-periodic solutions for all the planet's orbital eccentricities and inclinations as a function of time (Murray & Dermott, 2000). Laplace and Lagrange concluded that the Solar System would thus be forever stable, since a sum of periodic functions must repeat indefinitely. This so-called *secular* approximation (meaning slow, or long-term) is a key result in orbital dynamics and will be revisited in detail in Ch. 3.

While this secular approximation works well for certain orbital configurations, further scrutiny revealed that it falls apart for others. Poincaré (1899) was the first to discover that, even in the simpler three-body problem of a star and two planets, the solutions for some orbital configurations are extremely sensitive to small changes in the initial conditions. He uncovered the dynamical behavior we now call chaos. Poincaré realized that this precludes the possibility of finding an analytical solution to the three-body problem, as any analytical solution assumes that the answer depends smoothly on the initial configurations. Chaotic systems defy this expectation. Hidden within the small terms ignored by Laplace and Lagrange's leading-order expansion lay the seeds of this perplexing behavior.

Importantly, chaos also opens up the possibility of dynamical instabilities and collisions over long timescales. While quasi-periodic solutions are restricted to repeatedly traversing the same surfaces in phase space indefinitely, chaotic solutions can explore much wider regions of phase space over time (Lichtenberg & Lieberman, 2013). This allows orbits to evolve to the point where they become sufficiently eccentric to cross one another, leading to the instabilities and collisions that underlie the planet formation process.

These surprises in classical mechanics motivated efforts to understand the conditions under which chaos can arise. Rigorous efforts in the area of applied math culminated in the celebrated KAM theorem (Kolmogorov, 1954; Arnol'd, 1963a,b; Moser, 1973). In the margins of a letter from Vladimir Arnold in 1965, Michel Hénon applied these new results to the planetary problem (Laskar, 2014). In this context, the KAM theorem asks, if one started with a massless 'Earth' orbiting the Sun, and then dialed up the mass of a perturbing 'Jupiter' starting from zero, how massive could one make Jupiter while guaranteeing that the Earth's orbital solution remains quasi-periodic and not chaotic? Amusingly, Hénon's shows that quasi-periodicity can be guaranteed as long as the mass of 'Jupiter' is smaller than $\sim 10^{-259}$ the mass of an electron (Hénon, 1965). Rigorous mathematical theorems have thus had limited practical use for understanding chaos in planetary dynamics.

1.3 Stability in the Three-body Problem

One widely applicable insight is that chaos under conservative forces always arises due to the existence of resonances, or integer ratios between different frequencies in the system (Lichtenberg & Lieberman, 2013). However, identifying the particular resonances dominantly responsible for driving chaos is not necessarily straightforward. In the planetary context, there are many candidates to consider. These include resonances between the rates at which different planets orbit their host star, known as mean motion resonances (MMRs), ones between the slower rates at which the pericenters precess (rotate), ones between the rates at which the orbital planes precess, as well as any combination of these three.

In the case of two planets on closely spaced orbits (i.e., the three-body problem), Wisdom (1980) showed that the stability boundary is determined specifically by MMRs between the orbital periods. The theory is illustrated in Fig. 1.1. As the separation between the two planets varies (along the x-axis), MMRs occur whenever their orbital periods are close to integer ratios (x-axis ticks). The planets do not have to have *exactly* an integer ratio to be in resonance—there is a finite range of period ratios around each MMR (shaded gray) in which the pair of planets could start, and the period ratio would still oscillate around that integer ratio. The extent of this region is referred to as the width of the resonance. The width is effectively set by how strong the gravitational interaction between the two planets is, relative to the dominant gravitational force from the central star. In particular, the widths increase as the planets become more massive, and as the orbits become more eccentric (which causes them to have closer, stronger gravitational encounters). This is why the widths, or domains of influence, of each MMR (in gray) get wider as the eccentricity increases along the y-axis (the eccentricity has been normalized by the value at which the eccentricities cross so, at the top of the plot, the orbits intersect).

One of the few useful heuristic criteria for chaos in conservative systems is the so-called resonance overlap criterion (Chirikov, 1979). Rather than trying to map chaotic regions in detail, it states that the transition from mostly quasi-periodic to mostly chaotic behavior corresponds to the boundary where adjacent resonances start overlapping one another (solid red line in Fig. 1.1) (Hadden & Lithwick, 2018). We review the dynamics of MMRs and this resonance overlap criterion in more detail in Ch. 2.

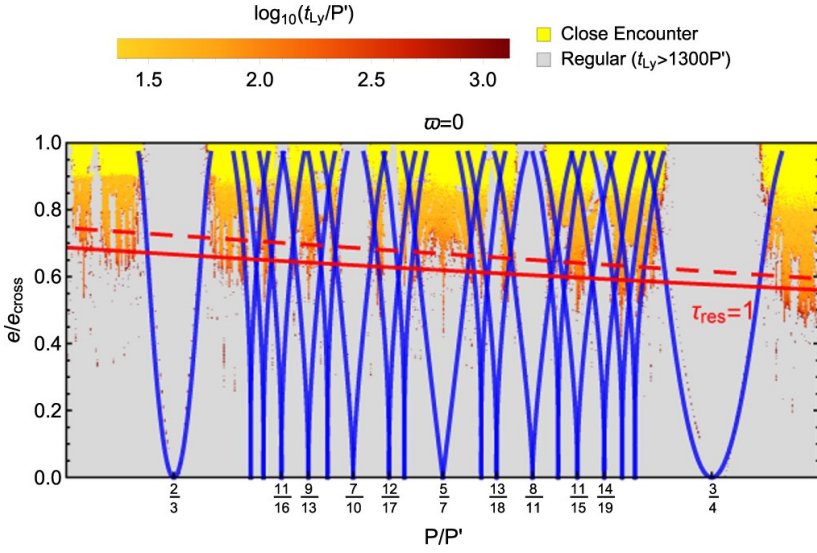


Figure 1.1: Structure of resonances and their overlap between the 3:2 and 4:3 MMRs for an eccentric test particle perturbed by a planet on an exterior circular orbit, copied from (Hadden & Lithwick, 2018). The x-axis shows the ratio of the test particle's orbital period P to the period of the planet P' . The y-axis plots the eccentricity of the test particle, normalized by its orbit-crossing eccentricity $e_{\text{cross}} \equiv 1 - a/a'$, where a and a' are the semimajor axes of the test particle and the planet. The MMRs in blue become wider as the test particle's eccentricity increases and eventually overlap with their neighboring MMRs. The stability boundary, beyond which the system is always chaotic (orange regions), is well-approximated by the red line at which the MMRs start to overlap.

1.4 Extending to Multiplanet Systems

1.4.1 Numerical Work

Unfortunately, we know that most planetary systems have more than two planets (Zhu et al., 2018), and the introduction of a third planet (or more) yields qualitatively different dynamical behavior. This defied further analytical progress and led to almost three decades of research involving running large suites of numerical integrations, systematically varying initial orbital parameters, and fitting empirical scaling laws for the time it takes systems to go unstable (Chambers et al., 1996; Marzari & Weidenschilling, 2002; Quillen & Faber, 2006; Obertas et al., 2017; Gratia & Lissauer, 2021).

These studies revealed that while in the two-planet case (Sec. 1.3), chaotic configurations quickly lead to close encounters and collisions in $\lesssim 100$ orbits, systems with three or more planets (i.e., multiplanet systems) exhibit instabilities over a much larger dynamical range of instability timescales and a significantly broader range of orbital parameters compared to two-planet systems.¹

Nevertheless, the qualitatively different behavior of multiplanet systems must still ultimately be attributable to the action of particular resonances (Sec. 1.3), despite that there was little agreement on which. A convincing clue was provided by a suite of integrations of initially circular, coplanar and equally spaced five-planet systems by Obertas et al. (2017) (Fig. 1.2). As one might expect, increasing the spacing between planets on the x-axis leads to an increase in the time to instability (measured in orbital periods) on the logarithmic y-axis. However, superimposed on this general trend are several sharp dips, in some cases by several orders of magnitude, at spacings corresponding to MMRs between adjacent planets (indicated by vertical solid and dashed lines). This suggested that MMRs are likely still involved as in the three-body problem (Sec. 1.3), though the qualitatively different behavior suggests that the instability mechanism is more complicated.

1.4.2 Analytical Work

Two dynamical mechanisms have been recently proposed to explain instabilities in compact multiplanet systems. The first is that three-body resonances resulting from interactions between trios of planets are the fundamental source of chaos in systems (even for the ones with more than three planets) with closely spaced orbits (Rath et al., 2022). The second suggests that the above picture

¹The terms ‘chaotic’ and ‘unstable’ can thus be used interchangeably in practice. For multiplanet systems, chaotic configurations might take a long time to go unstable. However, the instability timescales for chaotic, compact configurations are typically still much shorter than the Gyr lifetimes of planetary systems, so for simplicity, this thesis will use the two terms interchangeably despite some technical differences.

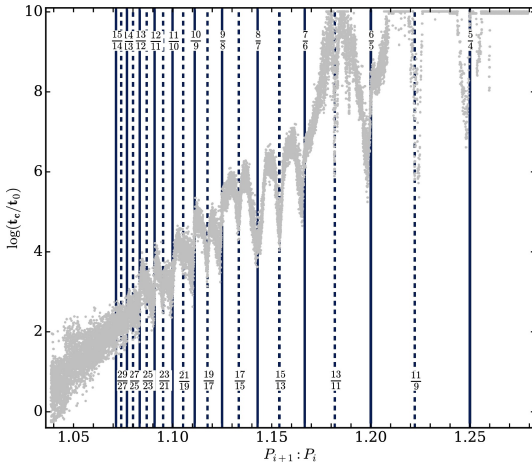


Figure 1.2: Stability times of systems with five Earth-mass planets as a function of the initial separation between planets, copied from (Obertas et al., 2017). Vertical lines show the locations of first-order (solid) and second-order (dashed) MMRs between adjacent planets. We see a sharp decrease in survival times when planets are close to the MMRs.

of MMR overlap between individual pairs of planets still holds; however, the boundary in Fig. 1.1 becomes time dependent due to long-term, secular variations mentioned in Sec. 1.2 (Tamayo et al., 2021b).

This thesis focuses on the latter hypothesis (we briefly discuss the former in Appendix A). Because the widths of the MMRs depend on the eccentricity, long-term oscillations in eccentricity will lead to the continuous expansion and contraction of MMR widths. In Fig. 1.3, we fix the initial eccentricity along the y-axis and plot snapshots of the extents of MMRs over one secular cycle. Because the resonances expand and contract, the line where the MMRs start overlapping is no longer static. The stability boundary should therefore be determined by the location of maximum overlap (right-most panel). Tamayo et al. (2021b) calculated the extent of these secular variations and the associated stability boundary numerically, demonstrating good agreement with N-body integrations.

However, without closed-form, analytical expressions for these quantities, we do not understand the particular combinations of parameters dominantly driving the dynamics, nor how the stability boundary scales with these variables. Analytically deriving such results would allow us to reduce and visualize the otherwise high-dimensional parameter space, identify the key directions setting stability, and clarify the degeneracies inherent to stability constraints. Perhaps most importantly, a simple closed-form expression for the stability boundary would be much more widely used by the community than the numerical matrix diagonalization procedure outlined by Tamayo et al. (2021b).

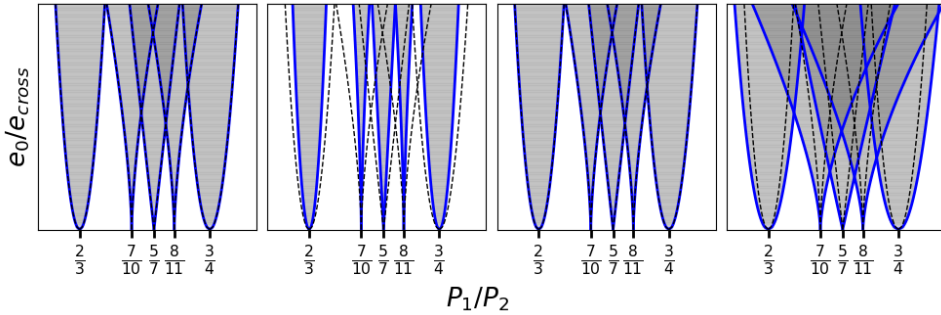


Figure 1.3: MMRs expand and contract over the secular timescale. We define the y-axis to be the initial eccentricity of the test particle (normalized by its orbit-crossing eccentricity), and we plot snapshots of the MMR widths over time. The stability boundary should correspond to the location of maximum MMR overlap.

1.5 Outline

The goal of this thesis is thus to develop an analytical expression for the stability boundary, under the secular eccentricity evolution described above. We begin by providing a self-contained introduction to the dynamics of MMRs in Ch. 2. In Ch. 3, we present a novel, leading-order approximation for the secular dynamics of compact, coplanar three-planet systems, recently accepted for publication in the *Astrophysical Journal* (Yang & Tamayo, 2023). This provides not only analytical expressions, but also geometric intuition into the conserved eigenmodes driving the dynamics, with a wide range of applications beyond questions of stability. In Ch. 4, we present a simple expression for the expansion and contraction of MMRs and discuss a method for calculating the stability boundary at the extremum in the secular evolution where resonances are widest. We obtain an expression for the resulting stability boundary and finally test it against a suite of numerical simulations. We conclude with a summary of the main results, as well as future avenues opened by this work.

Chapter 2

Two-body MMRs

2.1 The Physics of Resonance

In a planetary system, the gravitational perturbations on a planet from its neighboring planet are orders of magnitudes weaker compared to the force from the central star. Moreover, these interactions typically take place at effectively random phases between the planets, and their effects are averaged out over time. However, when the orbital periods are near an integer ratio, the perturbations can build up coherently at the same phase to have important effects.

We say that two planets are in a mean motion resonance (MMR) if their orbital periods are close enough to an integer ratio (gray regions in Fig. 1.1). Depending on the initial configurations, MMRs can be a powerful stabilizing or destabilizing force in a planetary system. To illustrate such behaviors, we consider a planar two-planet system in a 2:1 resonance. For simplicity, we have a planet in a fixed circular orbit and a test particle (e.g., an asteroid) on an interior, coplanar, eccentric orbit. In this setup, the circular orbit of the planet never changes, and we can focus on the dynamics of the test particle. The closest approach between the two orbits, which is where the pair interact the most strongly with each other, takes place at the aphelion of the test particle where it is farthest from the star (left-most snapshot in Fig. 2.2).

First we illustrate two equilibrium configurations where the conjunctions between the pair always take place at the same longitude. (i) At the stable equilibrium, the system starts with the two bodies in conjunction at the test particle's perihelion. In Fig. 2.1, we show snapshots of the relative positions of the test particle and the planet within one orbital period of the planet. When the test particle is at the longitude of closest approach, the planet will be 90° away; when the planet is around the longitude of close approaches, the test particle will be 180° away. The close approaches between orbits are avoided by the resonant mechanism, and the system stays at the stable equilibrium. (ii) At the unstable equilibrium, the test particle and the planet are in conjunction at the test par-

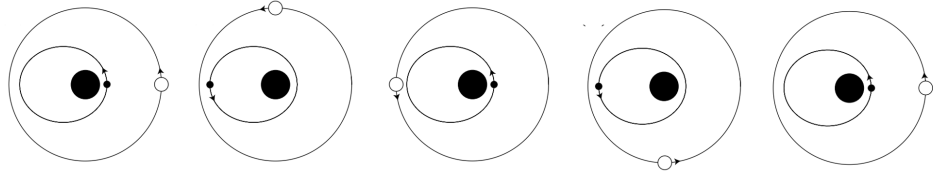


Figure 2.1: Stable configuration between the test particle and the planet in a 2:1 resonance over one orbital period of the planet, copied from (Murray & Dermott, 2000). The conjunctions take place at the longitude of furthest approach.

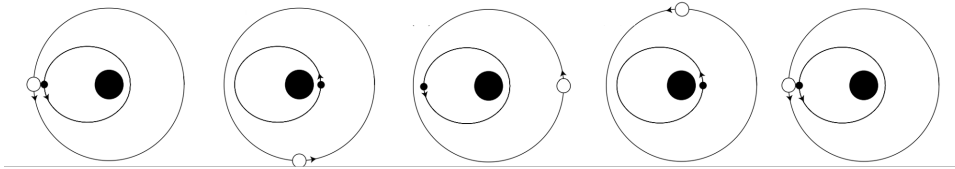


Figure 2.2: Unstable configuration for the test particle and the planet in a 2:1 resonance over one orbital period of the planet, copied from (Murray & Dermott, 2000). The conjunctions take place at the longitude of closest approach.

ticle's aphelion (Fig. 2.2). The system will quickly destabilize since the closest approach is repeated every orbital period of the planet.

In the equilibrium configurations above, the conjunctions take place either at the perihelion or the aphelion. Due to orbital symmetry, the tangential force experienced by the test particle right before and after the conjunction is equal and opposite. Since there is no net tangential force, the angular momentum of the test particle is conserved (Murray & Dermott, 2000). However, this symmetry is broken if conjunctions occur at other locations, and we examine its effect by analyzing the forces on the test particle right before and after conjunctions.

We consider the case where a conjunction occurs at point A or point D in Fig. 2.3. As the pair are diverging from each other, the magnitude of the pre-conjunction tangential force is larger than the post-conjunction one. The test particle ends up gaining angular momentum (or energy) and orbiting at a larger semimajor axis with lower rate. The subsequent conjunctions will take place closer to the perihelion, or the longitude of farthest approach. When the conjunction happens after the farthest approach (e.g. at point B and C in Fig. 2.3), the test particle will experience a net loss in energy and start orbiting at a faster angular velocity. The subsequent conjunctions will then take place before the previous one, closer to the perihelion. Therefore, for two bodies at resonance with arbitrary initial conditions, we expect their conjunction angle to oscillate around the perihelion, or the longitude of farthest approach.

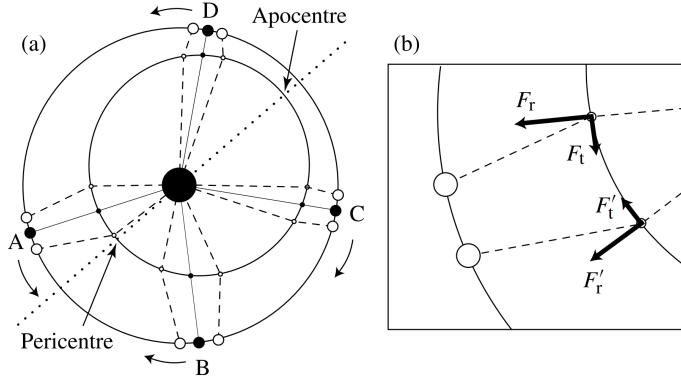


Figure 2.3: Schematic diagram of resonant encounters between an eccentric test particle and a planet on an exterior circular orbit, copied from (Murray & Dermott, 2000). Panel (a) illustrates the geometry of conjunctions at four different longitudes. The arrows show the directions towards which consecutive conjunctions should be moving. Panel (b) shows the pre- and post-conjunction forces on the test particle at point A. Since the pair are moving towards larger separation, the tangential force on the test particle is larger before the encounter.

The stable and unstable equilibrium configurations above are commonly analogized to those of a pendulum. A pendulum hanging straight down is stable to additional perturbations and will simply oscillate around the stable equilibrium point. In contrast, an inverted pendulum is in an unstable configuration, since the slightest perturbation is enough to make it fall one way or another. As long as the eccentricities are not too small, the dynamics between a test particle and a planet near an MMR is well-approximated by the Hamiltonian for a pendulum:

$$\mathcal{H} = \frac{1}{2}\dot{\phi}^2 - \epsilon \cos\phi, \quad (2.1)$$

where ϕ denotes the longitude of conjunction from the farthest approach, and ϵ is dependent on the mass of the planet and the eccentricity of the test particle (Rath et al., 2022).

So the resonant dynamics in a two-planet system can be characterized by a phase space portrait similar to that of a pendulum as we show in Fig. 2.4. Each trajectory on the graph corresponds to one specific set of initial conditions. Chaos takes place at the boundary, or separatrix, of the cat's eye highlighted in blue. It separates the motion of the conjunction angles between bounded oscillations around the stable equilibrium (which is the point of farthest approach) and unbounded circulations around the whole orbit. This configuration at the separatrix is analogous to a pendulum with just the right amount of initial momentum to rotate until it rests upside down at the unstable equilibrium. Hence, the slight-

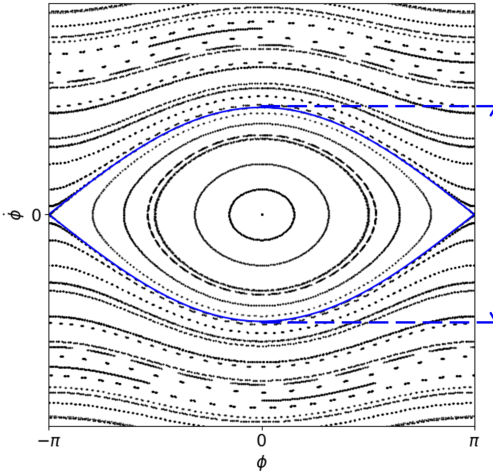


Figure 2.4: Phase space plot of a two-planet system described by the pendulum model in Eq. 2.1. Each trajectory corresponds to a specific set of initial conditions and consists of snapshots at every orbital period of the planet. The separatrix, or the chaotic zone, is highlighted in solid blue line. The arrow indicates the resonance width.

est perturbation to a system around the separatrix can cause it to either oscillate back or circulate (like the pendulum going over the top). This strong sensitivity to external perturbations is the hallmark of chaos, and explains why resonances are generically responsible for driving chaos in conservative systems (Lichtenberg & Lieberman, 2013). The most vulnerable trajectories to chaos are always the resonance separatrices, which we will discuss in the next subsection.

The overall width of the separatrix, indicated by the blue arrow in Fig. 2.4, is known as the resonance width. The resonance width depends on how strongly the test particle and the planet interact – it increases with the mass of the planet and the eccentricity of the test particle that determines the separation between the pair at their closest approach (Rath et al., 2022).

2.2 The Chaotic Boundary

The MMRs have finite widths that are dependent on the test particle's eccentricity. For each MMR, we can take a cut at $\phi = 0$ in the phase space plot (Fig. 2.4) and record the resonance extent as we vary the eccentricity of the test particle. We combine the results across all low-order resonances between the 3:2 and the 4:3 MMRs and plot them in Fig 2.5. The extent of each resonance is shaded in gray, and the blue boundaries correspond to the separatrices that have negligible widths. According to the pendulum model, chaos will take place right at the separatrix if the dynamics around the MMR is driven solely by that MMR itself. In reality, however, nearby MMRs also perturbs the motion and drives additional chaos around the separatrices (see Appendix A). As a result, there will be small chaotic layers of finite width (indicated in yellow) around the blue boundaries. These would be very thin toward the bottom where the perturbations from nearby resonances are small, but get stronger toward the top as the MMR regions grow in extent with increasing eccentricity.

Unfortunately, mapping the chaos due to perturbations from nearby MMRs in detail is challenging. A widely used heuristic criterion for widespread chaos is the locations at which neighboring MMRs start to overlap one another, marked by the dark gray regions in Fig. 2.5 (Chirikov, 1979; Hadden & Lithwick, 2018). We compare the stability boundary predicted by the MMR overlap criterion with

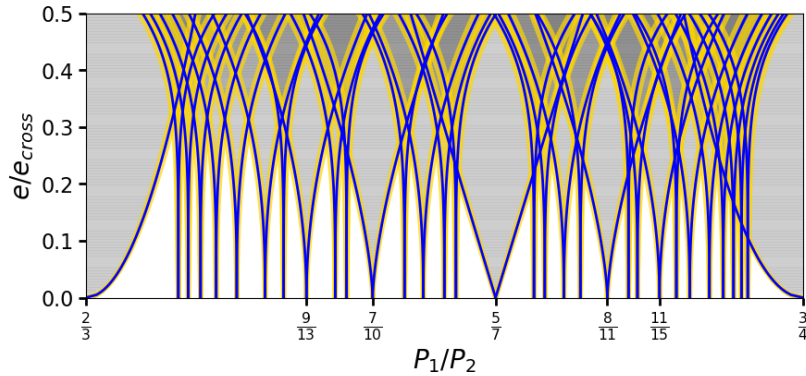


Figure 2.5: Structure of resonances between the 3:2 and the 4:3 MMRs. The extent of each resonance is shaded in gray, which increases with the test particle's eccentricity. We normalize the eccentricity along the y-axis by the orbit-crossing eccentricity $e_{\text{cross}} \equiv 1 - a_1/a_2$, where a_1 and a_2 are the semimajor axes of the test particle and the planet. The blue boundaries correspond to the separatrices, which have negligible widths. Perturbations from nearby MMRs will drive chaos around the separatrices and create small chaotic layers marked in yellow near the boundaries. The chaotic zones becomes thicker as eccentricity increases.

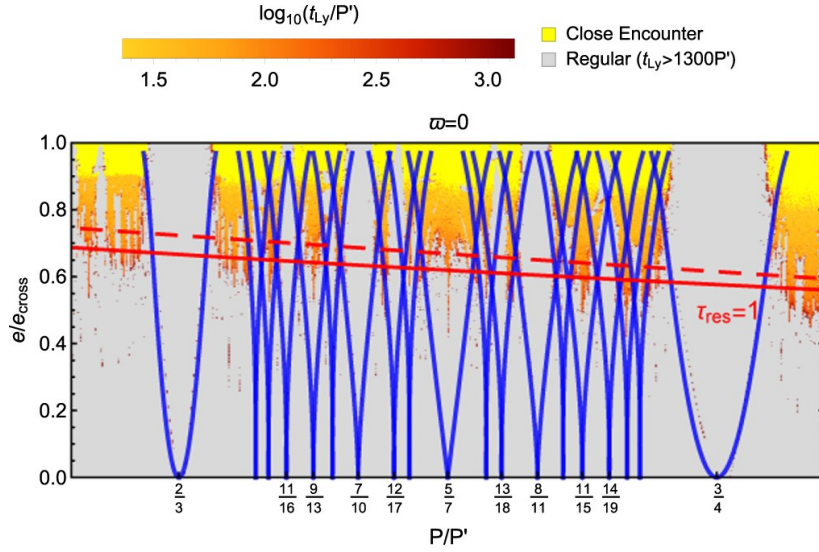


Figure 2.6: Chaotic structure in a system of a test particle subject to an exterior circular perturber, same as Fig. 1.1. The blue boundaries mark the separatrices of each MMR, and the solid red line shows the boundary at which MMRs start to overlap. The color scale shows the numerically computed Lyapunov time of chaotic trajectories – the gray regions are stable, and the orange regions are chaotic.

simulations in Fig. 2.6. We see that instability in the system is predominantly set by the MMR overlap, and it broadly agrees with the boundary at which MMRs start to overlap.

When we add a third planet (or more) to the system, the chaotic region grows as a result of the expansion and contraction of the MMRs (Fig. 1.3)¹. To make analytical progress, we therefore will first derive closed-form expressions for the long-term eccentricity oscillations driving this behavior (Ch. 3), and then obtain a solution for the resulting stability boundary (Ch. 4).

¹Also due to 3-body MMRs, see Appendix A for more discussions on this.

2.3 Generalizing to Two Eccentric Orbits

We assumed above a case of a test particle perturbed by a massive planet on a coplanar, circular orbit. This simplifies the problem, because then the unperturbed massive planet will indefinitely remain on a circular orbit, and one can focus on the lower-dimensional dynamical evolution of a single eccentric test particle. This is also a valuable problem to study because in the limit where the two orbits are closely spaced, the more general problem of two massive planets on eccentric orbits can be mapped to the simpler problem above.

The dynamics between two planets on closely spaced orbits is governed by their close approaches at conjunction when the inner planet overtakes the outer and their separation is minimized. In our discussion above, we consider the limiting case where an eccentric test particle is perturbed by a planet in an exterior circular orbit. Under this configuration, the location of closest approach corresponds to the perihelion of the test particle. As we make the outer planet eccentric, the orbital geometry, and thus the location of strongest interactions, will depend on the relative eccentricities and the relative longitudes of perihelion between the pair.

We can retain the same orbital geometry by making a proper translation in our reference frame. We define the eccentricity vector of each planet as

$$\mathbf{e}_i \equiv e_i \exp\{i\omega_i\}, \quad (2.2)$$

which can be thought of as a vector in the complex plane of magnitude e_i that points from the star towards the perihelion ω_i . To the leading order in eccentricities, an elliptical orbit becomes equivalent to a circular orbit offset from the central star by $a_i \mathbf{e}_i$, where a_i is the semimajor axis. As we show in Fig. 2.7, the point of closest approach lies along $a_2 \mathbf{e}_2 - a_1 \mathbf{e}_1$. In the compact limit where $|\Delta a/a| \ll 1$, the point of closest approach points towards the relative eccentricity $\mathbf{e}_{12} \equiv \mathbf{e}_2 - \mathbf{e}_1$.

Therefore, two compact systems will have the same orbital geometry as long as they have the same relative eccentricity. And the orbital dynamics should only be dependent on the evolution of the relative eccentricity. Our arguments in the previous sections will still hold for an eccentric planet once we make the replacement $\mathbf{e} \rightarrow \mathbf{e}_{12}$.

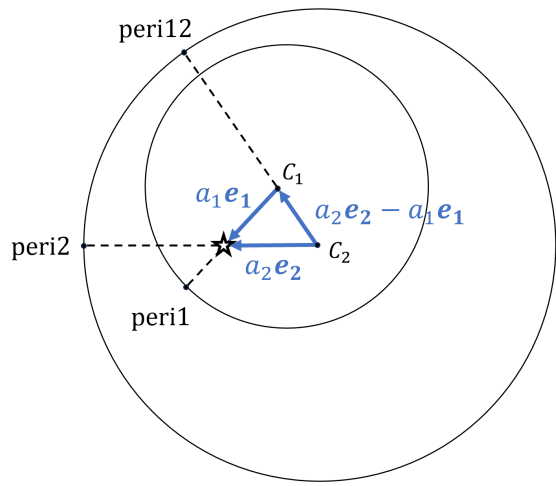


Figure 2.7: Schematic illustration of the eccentricity vectors. To leading order in eccentricities, each planet's orbit is a circle centered at C_i that is displaced from the central star by $a_i \mathbf{e}_i$, where a_i is the semimajor axis. The longitude of closest approach lies along the direction $a_2 \mathbf{e}_2 - a_1 \mathbf{e}_1$. In the compact limit, this quantity reduces to the relative eccentricity $\mathbf{e}_{12} \equiv \mathbf{e}_2 - \mathbf{e}_1$.

Chapter 3

Secular Dynamics

3.1 Overview

Secular variations in eccentricities cause the MMR widths to expand and contract, which could have a significant impact on the stability boundary. To quantify the modulation of the stability boundary, we want to develop an analytical expression for the secular evolution of eccentricities.

At low orbital eccentricities, and away from mean motion resonances (MMRs), the evolution of eccentricities in multiplanet systems behave approximately like a set of coupled harmonic oscillators. In an N -planet system, the seemingly complicated evolution of each planet's orbital eccentricity can thus be decomposed into N eccentricity eigenmodes that precess at constant eigenfrequencies. While this so-called Laplace-Lagrange solution is well known, it requires the numerical diagonalization of an $N \times N$ matrix, with complicated entries involving the planetary masses and special functions of the semimajor axis ratios (Murray & Dermott, 2000).

In this chapter, we obtain analytical solutions exploiting the limit where orbits are tightly spaced (Yang & Tamayo, accepted in the *Astrophysical Journal*). This compact limit is important for understanding the onset of instabilities in young planetary systems, which we expect to form with closer orbital separations and undergo a giant impact phase (e.g., Hansen & Murray, 2013; Tremaine, 2015; Dawson et al., 2016) that sets the final masses and orbital architectures we observe today, (e.g., Volk & Gladman, 2015; Pu & Wu, 2015).

Tamayo et al. (2016) and Tamayo et al. (2020) posited that even in compact systems with higher multiplicities, adjacent trios of planets provide the fundamental building block with which to understand stability, so this is the case we focus on in this chapter. As mentioned above, Tamayo et al. (2021b) showed that the long-term secular oscillations in the eccentricities discussed above cause the widths of MMRs to adiabatically breathe in and out, modulating the boundary at which MMRs overlap and drive widespread chaos. This should in principle

happen for two-planet systems too, but the particular combination of eccentricities that sets the MMR widths (e_{12} , see Ch.2.3) approximately coincides with one of the Laplace-Lagrange modes (i.e., one of the eigenmodes) that is conserved, so this effect only appears for 3+ planet systems (see Sec. 3.3).

This motivates better understanding the secular dynamics of three-planet systems. On one level, this problem was solved centuries ago. However, the matrix diagonalization is typically performed numerically (Van Laerhoven & Greenberg, 2012), because the general solution for the eigenvectors and eigenfrequencies in terms of the masses and orbital separations would span an entire page, and is thus of little use for applications. To make analytical progress, Tamayo et al. (2021b) studied the dynamics in the limit where two closely spaced planets are perturbed by a distant third body. However, this approximation is of limited use given that typical planetary systems have a tendency toward uniform spacings (Weiss et al., 2018).

In this chapter we seek more general results, driven by the expectation that the expressions should nevertheless simplify significantly in the compact limit. At close separations, where the eccentricities are necessarily small to avoid orbit-crossing, one can linearize the planets' unperturbed two-body paths following the “guiding-center approximation” (Murray & Dermott, 2000). This implies that only a particular linear combination of the eccentricity vectors determines the relative motion (Namouni et al., 1996), leading to an additional conserved quantity (Goldreich & Tremaine, 1981; Hénon & Petit, 1986). This insight has provided significant simplification and intuition for MMR dynamics (Hadden, 2019), and we show it similarly elucidates the secular problem. We will focus on the compact regime where the Laplace-Lagrange solution approximates the true dynamics, i.e., when the eccentricities are not only $\ll 1$, but additionally are small compared to the eccentricities at which the orbits would cross; the case of nearly crossing eccentricities is analyzed in the context of narrow planetary rings by Goldreich & Tremaine (1979).

We begin in Sec. 3.2 by introducing our Hamiltonian approach and applying it to the two-planet case following Tamayo et al. (2021b). We then use this intuition to guide the development of the three-planet case in Sec. 3.4. We derive a solution in the compact limit where the middle planet is much less massive in Sec. 3.4.1, and then explore how this result generalizes to wider separations in Sec. 3.4.2 and to massive middle planets in Sec. 3.4.3. We provide a sample application and comparison to N-body in Sec. 3.4.4.

3.2 Hamiltonian Laplace-Lagrange Formalism

At low inclinations typical of transiting planets, the stability of compact systems is not particularly sensitive to the inclination degrees of freedom (Tamayo et al., 2020, 2021b). We therefore model the system as a coplanar. Because the degrees of freedom corresponding to the semimajor axes are conserved in the secular problem (Murray & Dermott, 2000), there are N degrees of freedom for the eccentricity of each planet to consider.

We adopt canonical Poincaré variables, with actions and conjugate angles given by

$$\Gamma_i = m_i \sqrt{GM_\star a_i} \left(1 - \sqrt{1 - e_i^2} \right) \leftrightarrow \gamma_i = -\varpi_i \quad (3.1)$$

where G is the gravitational constant, M_\star the stellar mass, the m_i are the planetary masses, and the a_i , e_i and ϖ_i are the orbital semimajor axes, eccentricities and longitudes of pericenter, respectively. To make our expressions easier to manipulate, we adopt the complex variables

$$\mathbf{G}_i \equiv \sqrt{2\Gamma_i} e^{i\gamma_i}. \quad (3.2)$$

Note that at low eccentricities,

$$\mathbf{G}_i \approx \Lambda_i^{1/2} \mathbf{e}_i^*, \quad (3.3)$$

where $\Lambda_i \equiv m_i(GM_\star a_i)^{1/2}$, and the complex eccentricity

$$\mathbf{e}_i = e_i e^{i\varpi_i}, \quad (3.4)$$

can be thought of as a vector in the complex plane of magnitude e_i that points in the direction of pericenter ϖ_i .

In the compact limit where the a_i are approximately equal, the complex variables \mathbf{G}_i become approximately proportional to $\sqrt{\tilde{m}_i} \mathbf{e}_i$, where throughout the paper we define $\tilde{m}_i \equiv m_i/m_{tot}$ as the fraction of the total planetary mass.¹

Introducing a column vector of all the actions $\mathbf{G} \equiv (\mathbf{G}_1, \dots, \mathbf{G}_N)^T$, the Laplace-Lagrange Hamiltonian can be written as a compact matrix product,

$$\mathcal{H} = -\frac{1}{2} \mathbf{G}^T \cdot \mathcal{M} \cdot \mathbf{G}^*, \quad (3.5)$$

where \mathcal{M} is an $N \times N$ matrix with real entries involving the planetary masses and Laplace coefficients (we derive the three-planet case in Appendix B, see Eq. B.6).

¹To obtain more accurate expressions by considering a_i as different, we can re-define the dimensionless mass \tilde{m}_i in all the equations as $\tilde{m}_i \equiv m_i \sqrt{a_i} / \sum_{j=1}^N m_j \sqrt{a_j}$.

The N equations of motion are then given by

$$\frac{d}{dt} \mathbf{G} = -i\mathcal{M} \cdot \mathbf{G}. \quad (3.6)$$

When expressed in terms of canonical variables (rather than orbital elements, e.g., Murray & Dermott 2000), the Laplace-Lagrange matrix \mathcal{M} becomes symmetric, making it clear through the spectral theorem that one can find a rotated basis in which the matrix is diagonal with real eigenvalues.²

The diagonalizing rotation matrix \mathcal{R} yields variables

$$\mathbf{S} = \mathcal{R} \cdot \mathbf{G}, \quad (3.7)$$

which are the Laplace-Lagrange modes, with magnitudes set by initial conditions that remain constant and rotate in phase at the corresponding eigenfrequencies along the diagonal entries of $\mathcal{D} = \mathcal{R} \cdot \mathcal{M} \cdot \mathcal{R}^T$.

This provides a valuable geometrical picture where the evolution of each \mathbf{G}_i is given as a vector sum of contributions from these uniformly rotating modes (see Sec. 3.3 and Fig. 3.1).

We will repeatedly exploit the fact that for compact systems, the “center-of-mass eccentricity” $\mathbf{e}_{com} = \sum_{i=1}^N \dot{m}_i \mathbf{e}_i$ is conserved (Goldreich & Tremaine, 1981). As we show explicitly in Eq. 3.17, this implies that $\mathbf{S}_{com} \propto \mathbf{e}_{com}$ is always an eigenmode of a compact N -planet system with zero eigenfrequency (i.e., its magnitude and direction are conserved). This is similar to the two-body problem, where the center-of-mass degree of freedom is conserved and one can reduce to an equivalent one-body problem.

3.3 Compact Two-planet Systems

Tamayo et al. (2021b) showed that in the compact limit for 2 planets, if we approximate the semimajor axes as equal,

$$\begin{pmatrix} \mathbf{S}_{12} \\ \mathbf{S}_{com} \end{pmatrix} \approx - \begin{pmatrix} \sqrt{\frac{m_2}{m_1+m_2}} & -\sqrt{\frac{m_1}{m_1+m_2}} \\ \sqrt{\frac{m_1}{m_1+m_2}} & \sqrt{\frac{m_2}{m_1+m_2}} \end{pmatrix} \begin{pmatrix} \sqrt{m_1} & 0 \\ 0 & \sqrt{m_2} \end{pmatrix} \begin{pmatrix} \mathbf{e}_1^* \\ \mathbf{e}_2^* \end{pmatrix} = \begin{pmatrix} \sqrt{\frac{m_1 m_2}{m_1+m_2}} \mathbf{e}_{12}^* \\ -\sqrt{m_1 + m_2} \mathbf{e}_{com}^* \end{pmatrix} \quad (3.8)$$

where $\mathbf{e}_{12} \equiv \mathbf{e}_2 - \mathbf{e}_1$. Inverting this equation to express the \mathbf{G}_i as a sum of the constant modes becomes ill-defined in the test particle limit where one of the planet masses vanishes and $\mathbf{S}_{12} \rightarrow 0$. The eccentricities nevertheless remain well behaved. Since \mathcal{R} is a rotation matrix (so $\mathcal{R}^{-1} = \mathcal{R}^T$), we have from Eq. 3.8

²In the notation of the `celmech` package, the real and imaginary components of the G_i correspond to (η_i, κ_i) . The `celmech` Laplace-Lagrange example uses variables $x_i = G_i^*/\sqrt{2}$. This leads to a different form of Hamilton’s equations, but both sets of variables yield the same differential equation (Eq. 3.6) with the same matrix \mathcal{M} . The elements of \mathcal{M} in the Appendix (Eq. B.6) can therefore still be directly compared with those from the `celmech` package.

$$\begin{pmatrix} \mathbf{e}_1 \\ \mathbf{e}_2 \end{pmatrix} \approx \begin{pmatrix} \frac{1}{\sqrt{m_1}} & 0 \\ 0 & \frac{1}{\sqrt{m_2}} \end{pmatrix} \mathcal{R}^T \begin{pmatrix} \sqrt{\frac{m_1 m_2}{m_1 + m_2}} & 0 \\ 0 & -\sqrt{m_1 + m_2} \end{pmatrix} \begin{pmatrix} \mathbf{e}_{12} \\ \mathbf{e}_{com} \end{pmatrix} = \begin{pmatrix} -\tilde{m}_2 \mathbf{e}_{12}(t) + \mathbf{e}_{com} \\ \tilde{m}_1 \mathbf{e}_{12}(t) + \mathbf{e}_{com} \end{pmatrix}. \quad (3.9)$$

Equation 3.9 provides the geometrical interpretation described at the end of Sec. 3.2, and is shown in Fig. 3.1. Both \mathbf{e}_1 and \mathbf{e}_2 have equal contributions of \mathbf{e}_{com} , which is conserved and maintains constant magnitude and direction. By contrast, the second mode³ $\mathbf{e}_{12} = \mathbf{e}_{12,0} e^{i\omega_{12} t}$ undergoes uniform rotation along the orange circle at a rate (Tamayo et al., 2021b)

$$\omega_{12} \approx \frac{m_{tot}}{M_\star} \frac{1}{e_{c,12}^2} \frac{1}{P_2}, \quad (3.10)$$

where P_2 is the outer planet's orbital period, and $e_{c,12}$ is the value of e_{12} at which the orbits would cross. For tightly packed orbits

$$e_{c,ij} = 1 - \alpha_{ij} = 1 - a_i/a_j \quad (3.11)$$

the secular timescale $T = 2\pi/\omega_{12}$ is typically quoted as $\sim (M_\star/m_{tot})P_2$ as appropriate for large crossing eccentricities (fractional separations), but we see that for compact systems, T is significantly reduced by a factor of $e_{c,12}^2$.

If we subtract both rows of Eq. 3.9, the common \mathbf{e}_{com} contribution cancels, and we self-consistently recover that $\mathbf{e}_2 - \mathbf{e}_1 = \mathbf{e}_{12}$. Thus, the relative eccentricity \mathbf{e}_{12} sweeps out a circle of constant radius, so the magnitude e_{12} is conserved (right panel of Fig. 3.1). This is a somewhat redundant argument given that we already found in Eq. 3.8 that \mathbf{e}_{12} was one of the modes (whose magnitudes are always conserved). But the fact that the relative eccentricity \mathbf{e}_{12} corresponds to one of the Laplace-Lagrange modes is specific to the compact two-planet case, where it has the important implication that there is no secular modification to MMR widths (Tamayo et al., 2021b).

In general, for compact N-planet systems with $N > 2$, it is no longer true that the relative eccentricities setting the MMR widths correspond to Laplace-Lagrange modes. However, we will show that the conservation of \mathbf{e}_{com} implies that all the eccentricities have approximately equal contributions of the \mathbf{e}_{com} mode, implying that in general, any relative eccentricities can only be made up of combinations of the remaining $N - 1$ modes.

³For ease of discussion, we will interchangeably refer to the mass-weighted canonical actions \mathbf{S} and their corresponding unweighted eccentricities (e.g., \mathbf{S}_{12} and \mathbf{e}_{12}) as “modes”.

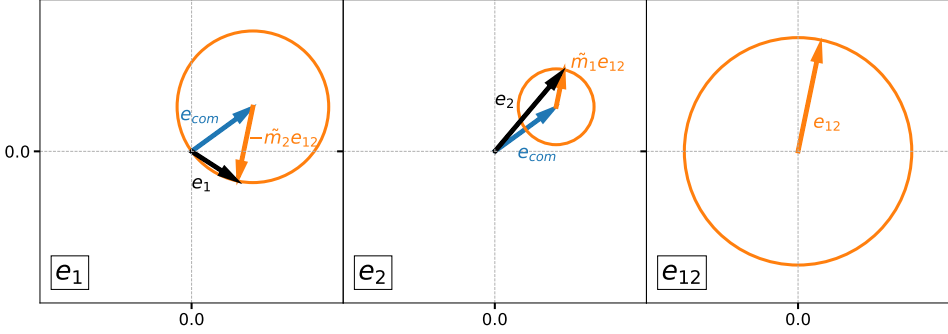


Figure 3.1: In a compact two-planet system, the eccentricities e_1 (left panel) and e_2 (middle panel) can be decomposed as the vector sum of contributions from the two Laplace-Lagrange eigenmodes e_{com} (blue) and e_{12} (orange). The magnitude and direction of e_{com} are conserved so the blue arrows remain fixed, while the e_{12} mode rotates uniformly at fixed magnitude along the orange circles. As this occurs, the magnitudes of e_1 and e_2 (black arrows) periodically grow and shrink, but because both share the same contribution from e_{com} , their relative eccentricity e_{12} is conserved (right panel). One can also see that the total e_{12} (right panel) gets split between the two eccentricities (left and middle panels) in proportion to the planetary masses.

3.4 Compact Three-planet Systems

3.4.1 Low-mass Limit

In the limit where the third planet in the middle is much less massive, the two massive planets still approximately undergo two-planet dynamics, so we know that two of the three eigenmodes are approximately those given above, i.e., e_{com} and e_{13} (note the changed index due to the additional middle planet). These specify the bottom two rows of our rotation matrix \mathcal{R}_1 .⁴ The requirement that \mathcal{R}_1 be orthogonal and have a determinant of unity in order to be a rotation uniquely determines the third eigenmode along the top row,

$$\mathcal{R}_1 = \begin{pmatrix} \sqrt{\frac{\tilde{m}_1 \tilde{m}_2}{\tilde{m}_1 + \tilde{m}_3}} & -\sqrt{\tilde{m}_1 + \tilde{m}_3} & \sqrt{\frac{\tilde{m}_2 \tilde{m}_3}{\tilde{m}_1 + \tilde{m}_3}} \\ -\sqrt{\frac{\tilde{m}_3}{\tilde{m}_1 + \tilde{m}_3}} & 0 & \sqrt{\frac{\tilde{m}_1}{\tilde{m}_1 + \tilde{m}_3}} \\ \sqrt{\tilde{m}_1} & \sqrt{\tilde{m}_2} & \sqrt{\tilde{m}_3} \end{pmatrix}, \quad (3.12)$$

⁴We set the middle entry of the second row in Eq. 3.12 to zero instead of being proportional to the small parameter \tilde{m}_2 , because we will find that e_{13} remains an eigenmode with a massive middle planet in the important limit where planets are evenly spaced. By doing so we also obtain a simple expression for the top row.

which yields three rotated variables

$$\begin{pmatrix} \mathbf{S}'_1 \\ \mathbf{S}'_2 \\ \mathbf{S}'_3 \end{pmatrix} = \sqrt{m_{tot}} \begin{pmatrix} \sqrt{\frac{\tilde{m}_2}{\tilde{m}_1 + \tilde{m}_3}} (\tilde{m}_3 \mathbf{e}_{23}^* - \tilde{m}_1 \mathbf{e}_{12}^*) \\ \sqrt{\frac{\tilde{m}_1 \tilde{m}_3}{\tilde{m}_1 + \tilde{m}_3}} \mathbf{e}_{13}^* \\ \mathbf{e}_{com}^* \end{pmatrix} \quad (3.13)$$

The new Hamiltonian is

$$\begin{aligned} \tilde{\mathcal{H}} &= (\mathbf{S}'_1 \quad \mathbf{S}'_2 \quad \mathbf{S}'_3) \cdot \mathcal{M}' \cdot \begin{pmatrix} \mathbf{S}'_1^* \\ \mathbf{S}'_2^* \\ \mathbf{S}'_3^* \end{pmatrix}, \\ \mathcal{M}' &= \mathcal{R}_1 \cdot \mathcal{M} \cdot \mathcal{R}_1^T, \end{aligned} \quad (3.14)$$

where \mathcal{M}' is the rotated Laplace-Lagrange matrix.

In the compact limit where α is close to unity, the Laplace coefficients in Eq. B.6 can be approximated as (Tamayo et al., 2021b)

$$b_{3/2}^{(m)}(\alpha) \approx \frac{2}{\pi(1-\alpha)^2}, \quad (3.15)$$

which is independent of m . We define a parameter δ to represent the fractional difference between the Laplace coefficients that appear in our Hamiltonian:

$$\delta \equiv \frac{b_{3/2}^{(1)}(\alpha_{ij}) - b_{3/2}^{(2)}(\alpha_{ij})}{b_{3/2}^{(1)}(\alpha_{ij})}. \quad (3.16)$$

Substituting Eq. 3.16 into Eq. 3.14, we can write the rotated Laplace-Lagrange matrix as

$$\mathcal{M}' = \begin{pmatrix} \omega'_1 & k & 0 \\ k & \omega'_2 & 0 \\ 0 & 0 & 0 \end{pmatrix} + \delta \omega'_1 \mathcal{M}_d, \quad (3.17)$$

where we provide the expressions for ω'_1 , ω'_2 and k in Appendix C. The elements in \mathcal{M}_d are $\mathcal{O}(1)$ or smaller, while $\delta \lesssim 0.15$ for planet pairs with $\alpha > 0.75$, and drops to zero as α approaches unity. We therefore drop this additional correction. This simplification is worst when $k = 0$ and the neglected terms are the main off-diagonal entries. Nevertheless, we will find that the fractional error in the eigenmodes due to this approximation remain $\lesssim 10\%$ for $\alpha_{13} > 0.75$ (see Fig. 3.4).

As long as the spacings between the two planets are comparable, we show in Appendix C that k is much smaller than the diagonal entries. Nevertheless, we now show that it is important to perform one more rotation to remove these small off-diagonal terms. This is easily achieved through a rotation

$$\mathcal{R}_2 = \begin{pmatrix} \cos \psi & -\sin \psi & 0 \\ \sin \psi & \cos \psi & 0 \\ 0 & 0 & 1 \end{pmatrix}, \quad (3.18)$$

where

$$\psi = \frac{1}{2} \tan^{-1} \left(\frac{2k}{\omega'_2 - \omega'_1} \right). \quad (3.19)$$

The corresponding diagonal matrix $\mathcal{M}'' = \mathcal{R}_2 \cdot \mathcal{M}' \cdot \mathcal{R}_2^T$, with eigenmodes and eigenfrequencies given by

$$\begin{pmatrix} \mathbf{S}_1 \\ \mathbf{S}_2 \\ \mathbf{S}_3 \end{pmatrix} = \begin{pmatrix} \cos \psi \mathbf{S}'_1 - \sin \psi \mathbf{S}'_2 \\ \sin \psi \mathbf{S}'_1 + \cos \psi \mathbf{S}'_2 \\ \mathbf{S}'_3 \end{pmatrix}, \quad (3.20)$$

$$\begin{pmatrix} \omega_1 \\ \omega_2 \\ \omega_3 \end{pmatrix} = \begin{pmatrix} \omega'_1 \cos^2 \psi + \omega'_2 \sin^2 \psi - k \sin 2\psi \\ \omega'_1 \sin^2 \psi + \omega'_2 \cos^2 \psi + k \sin 2\psi \\ 0 \end{pmatrix}. \quad (3.21)$$

Equation 3.20 helps clarify the issue. Even though $\psi \ll 1$ for a low-mass middle planet, we have from Eq. 3.13 that S'_2 is larger than S'_1 by a factor $\sim \sqrt{m_3/m_2} \gg 1$, so the two contributions to \mathbf{S}_1 above are in fact of the same magnitude, while $\mathbf{S}_2 = \mathbf{S}'_2$ to excellent approximation.

In this low-mass limit, plugging Eqs. C.5-C.7 into Eq. 3.19 for the angle ψ yields

$$\psi \approx \frac{k}{\omega'_2 - \omega'_1} \approx \sqrt{\tilde{m}_1 \tilde{m}_2 \tilde{m}_3} \left(\frac{\frac{1}{e_{c,23}^2} - \frac{1}{e_{c,12}^2}}{\frac{\tilde{m}_1 \tilde{m}_2 - \tilde{m}_3}{e_{c,23}^2} + \frac{\tilde{m}_2 \tilde{m}_3 - \tilde{m}_1}{e_{c,12}^2} + \frac{(\tilde{m}_1 + \tilde{m}_3)^2}{e_{c,13}^2}} \right). \quad (3.22)$$

In the compact limit where all $e_c \ll 1$, we can additionally make the approximation that $e_{c,12} + e_{c,23} = e_{c,13}$. We define

$$\eta \equiv \frac{e_{c,12}}{e_{c,13}} - \frac{e_{c,23}}{e_{c,13}}, \quad (3.23)$$

which acts as a spacing asymmetry parameter. For fixed inner and outer planet orbits, $\eta = -1$ corresponds to placing the middle planet's orbit all the way up against the inner planet's orbit, $\eta = +1$ up against the outer planet's orbit, and $\eta = 0$ at equal spacing. This also implies

$$\frac{e_{c,12}}{e_{c,13}} = \frac{1}{2}(1 + \eta), \quad \frac{e_{c,23}}{e_{c,13}} = \frac{1}{2}(1 - \eta). \quad (3.24)$$

We also define a parameter that accounts for the asymmetry in the mass distribution of the inner and outer planets:

$$\mu \equiv \frac{\tilde{m}_3 - \tilde{m}_1}{\tilde{m}_1 + \tilde{m}_3}. \quad (3.25)$$

Then Eq. 3.22 reduces to

$$\psi = -\frac{8\sqrt{\tilde{m}_2(1-\mu^2)}\eta}{3+6\eta^2+8\mu\eta-\eta^4} \quad (3.26)$$

When $\tilde{m}_2 \ll 1$, we have $\psi \ll 1$ and $|S'_1| \ll 1$ in Eq. 3.20, so $\sin \psi \approx \psi$ and $\cos \psi \approx 1$. After significant algebra, the three eigenmodes can be expressed as

$$\begin{pmatrix} S_- \\ S_+ \\ S_{com} \end{pmatrix} = \sqrt{m_{tot}} \begin{pmatrix} \sqrt{\tilde{m}_2} \mathbf{e}_-^* \\ \sqrt{\tilde{m}_1 \tilde{m}_3} \mathbf{e}_{13}^* \\ \mathbf{e}_{com}^* \end{pmatrix}, \quad (3.27)$$

where

$$\begin{aligned} \mathbf{e}_- &\equiv \frac{\chi_{23} \mathbf{e}_{23} - \chi_{12} \mathbf{e}_{12}}{\chi_{23} + \chi_{12}}, \\ \chi_{23} &= (1 + \eta)^3 (3 - \eta) (1 + \mu), \\ \chi_{12} &= (1 - \eta)^3 (3 + \eta) (1 - \mu). \end{aligned} \quad (3.28)$$

We can normalize the coefficients such that

$$\mathbf{e}_- = \tilde{\chi}_{23} \mathbf{e}_{23} - \tilde{\chi}_{12} \mathbf{e}_{12}. \quad (3.29)$$

Note that \mathbf{e}_{13} is equivalent to $\mathbf{e}_+ \equiv \mathbf{e}_{12} + \mathbf{e}_{23}$. The \mathbf{e}_{13} mode is thus the sum of the relative eccentricities, while the \mathbf{e}_- mode is a mass and spacing-weighted difference of the relative eccentricities. As illustrated in Fig. 3.2, the weights range from 0 to 1 and display inversion symmetry in the $\eta - \mu$ space. Intuitively, $\tilde{\chi}_{12}$ and $\tilde{\chi}_{23}$ are dimensionless measures of the gravitational interaction strengths between the inner pair and the outer pair. When the inner planet is much more massive ($\mu \rightarrow -1$) or much closer to the middle planet ($\eta \rightarrow -1$), the inner pair forms a two-planet “subsystem.” We see that $\tilde{\chi}_{12} \rightarrow 1$, $\tilde{\chi}_{23} \rightarrow 0$, and we retain the two-planet eigenmode $\mathbf{e}_- \rightarrow -\mathbf{e}_{12}$. Similarly for $\mu \rightarrow +1$ and $\eta \rightarrow +1$, $\mathbf{e}_- \rightarrow \mathbf{e}_{23}$. For the perfectly symmetric case where $\mu = 0$ and $\eta = 0$, \mathbf{e}_- reduces to $\mathbf{e}_{23} - \mathbf{e}_{12}$.

We can relate the eccentricity of each planet to the eigenmodes by $\mathbf{G} = (\mathcal{R}_2 \mathcal{R}_1)^T$. \mathbf{S} , which, following the procedure in Sec. 3.3, results in

$$\begin{pmatrix} \mathbf{e}_1 \\ \mathbf{e}_2 \\ \mathbf{e}_3 \end{pmatrix} = \begin{pmatrix} \mathbf{e}_{com} - \tilde{m}_3 \mathbf{e}_{13} \\ \mathbf{e}_{com} + \frac{1}{2} [(\tilde{\chi}_{23} - \tilde{\chi}_{12}) - (\tilde{m}_3 - \tilde{m}_1)] \mathbf{e}_{13} - \mathbf{e}_- \\ \mathbf{e}_{com} + \tilde{m}_1 \mathbf{e}_{13} \end{pmatrix}, \quad (3.30)$$

and

$$\begin{pmatrix} \mathbf{e}_{12} \\ \mathbf{e}_{23} \end{pmatrix} = \begin{pmatrix} \tilde{\chi}_{23} \mathbf{e}_{13} - \mathbf{e}_- \\ \tilde{\chi}_{12} \mathbf{e}_{13} + \mathbf{e}_- \end{pmatrix}. \quad (3.31)$$

We illustrate this low-mass solution in Fig. 3.3, analogous to Fig. 3.1. The top row of panels show the individual eccentricities as a vector sum of their constituent eigenmodes. All of them share the same contribution from \mathbf{e}_{com} , so this eigenmode disappears from the relative eccentricities along the bottom row of panels. Unlike in the two-planet case, however, the relative eccentricities between adjacent planets \mathbf{e}_{12} and \mathbf{e}_{23} are in general made up of the remaining two eigenmodes, causing the relative eccentricities to oscillate in time (see top panel of Fig. 3.7, corresponding to the same system).

We now explore how well these eigenmodes derived in the compact low-mass limit generalize to wider separations and massive middle planets.

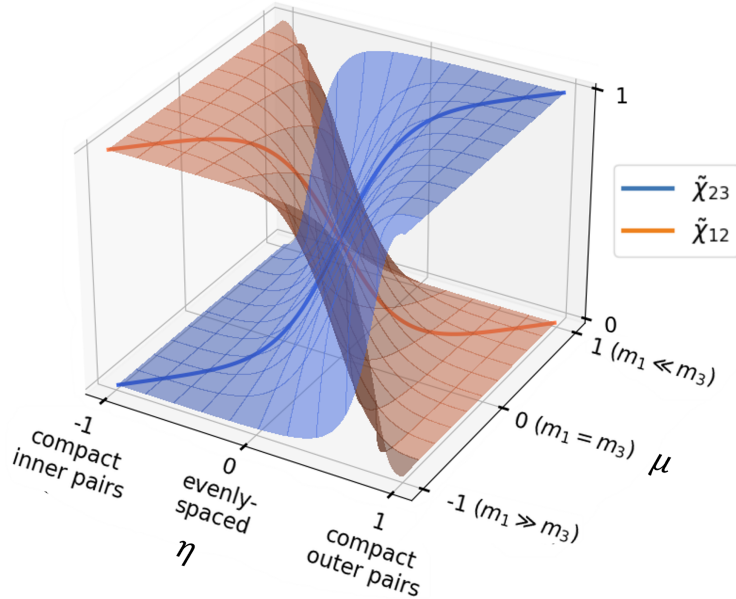


Figure 3.2: The values of $\tilde{\chi}_{12}$ and $\tilde{\chi}_{23}$ as a function of the mass distribution parameter μ and the spacing asymmetry parameter η . When the inner planet is significantly more massive or closer to the middle planet, the eigenmode e_- in Eq. 3.29 reduces to e_{12} , recovering the two-planet result. Similarly, for a massive outer planet that is closer to the middle planet, e_- reduces to e_{23} . When the inner and outer planets have equal masses and separations from the middle planet, e_- becomes the difference of the relative eccentricities $e_{23} - e_{12}$.

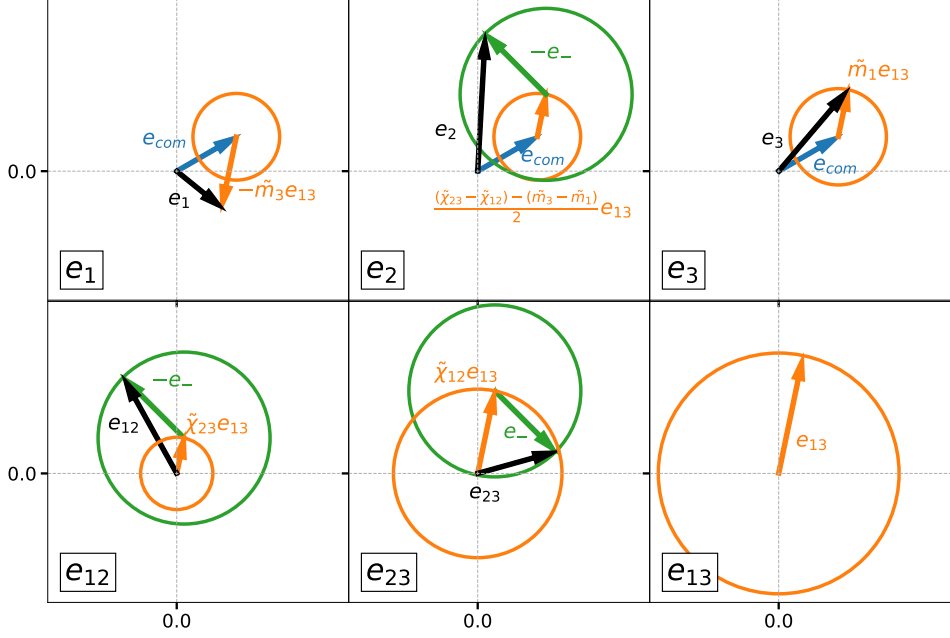


Figure 3.3: Analogous plot to Fig. 3.1, for a compact three-planet system where the middle planet is massless. The two massive planets then follow two-planet dynamics (compare the top left, top right and bottom right panels to Fig. 3.1). Again, all eccentricities share the same contribution from e_{com} (blue), so the relative eccentricities in the bottom row of panels are independent of this eigen-mode. However, unlike in the two-planet case, the relative eccentricities between adjacent planets e_{12} (bottom left panel) and e_{23} (bottom middle) are now in general governed by two eigenmodes and undergo oscillations, unlike the two-planet case.

3.4.2 Generalization to Wider Spacings

We first explore the effect of wider spacings by varying $\alpha_{13} = a_1/a_3$ along the x axis, considering uniformly spaced planets $\eta = 0$ with a massless middle planet. To quantify the error, we use the `celmech` package (Hadden & Tamayo, 2022) to numerically evaluate our Laplace-Lagrange matrix (Eq. B.6). We then diagonalize it numerically to obtain the true e_- , and normalize it to a unit vector. We then calculate our approximated unit vector for e_- using Eq. 3.29, and calculate the distance between our approximated unit vector and the true one. We show the result in Fig. 3.4, overplotting some separations corresponding to MMRs between adjacent planets. We see that for closer separations than the 3 : 2 (between adjacent planets), the error is $\lesssim 10\%$.

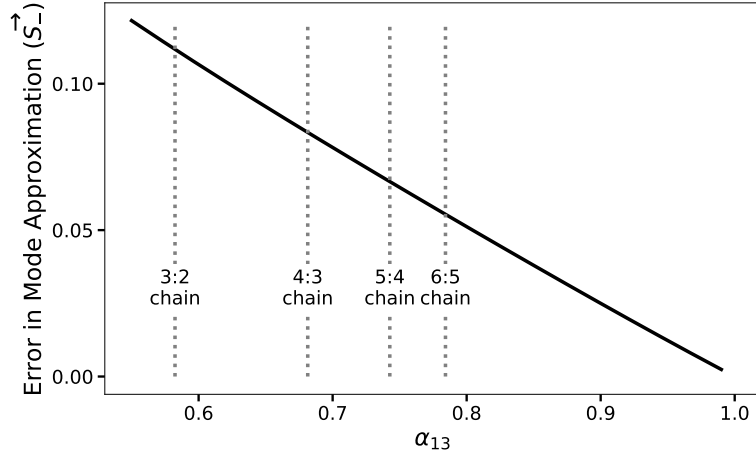


Figure 3.4: Error (as defined in the text) for our compact approximation of the e_- eigenmode (Eq. 3.29), considering an equally spaced ($\eta = 0$) three-planet system with a massless middle planet. On the x -axis we vary the ratio between the innermost and outermost semimajor axes, so that the compact approximation worsens moving left. Vertical dotted lines correspond to separations where the period ratios between adjacent planets falls on different first-order MMRs. The error is $\lesssim 10\%$ for period ratios between adjacent planets closer than the 3 : 2.

3.4.3 Generalization to Massive Middle Planets

When the middle planet is massive, there are additional terms $\propto \tilde{m}_2$ in the rotational angle ψ (Eq. 3.19) given by Eqs. C.5-C.7. If the rotation angle is still small, $\cos \psi \approx 1$ and $\sin \psi \approx \psi$ with

$$\psi \approx -\frac{8\sqrt{\tilde{m}_2(1-\mu^2)}\eta}{(3+6\eta^2+8\mu\eta-\eta^4)-\tilde{m}_2(3+6\eta^2-8\mu\eta-\eta^4)}. \quad (3.32)$$

After significant algebra, this yields a corrected mode

$$\mathbf{e}_-^{(1)} = \mathbf{e}_- + \frac{4}{\chi_{12} + \chi_{23}} \tilde{m}_2 \eta [(1+\mu)^2 \mathbf{e}_{23} + (1-\mu)^2 \mathbf{e}_{12}]. \quad (3.33)$$

As expected, the correction vanishes as $\tilde{m}_2 \rightarrow 0$ in the test particle limit.

Surprisingly, however, it also vanishes as $\eta \rightarrow 0$. Uniformly spaced three-planet systems thus share the same eigenmodes (but not eigenfrequencies) as the test particle case. This is visible in Fig. 3.5, where we plot the error in our low-mass mode (Eq. 3.29) as a function of the spacing asymmetry parameter η , with different color curves corresponding to different masses for the middle planet. To isolate this effect, we consider $\alpha_{13} = 0.99$ where the errors from the compact approximation are negligible (Fig. 3.4). In orange we plot the test particle case, which has small errors throughout. As the middle planets becomes progressively more massive (reaching the equal-mass case in purple), the errors grow in a V shape at small η , corresponding to the $\tilde{m}_2 \eta$ scaling of the correction in Eq. 3.33. If we include the correction, we find that we indeed fix the errors for $|\eta| \lesssim 0.1$; however, at larger η , our small-angle approximation for ψ becomes poor, and including this correction gives the wrong asymptotic behavior as $|\eta| \rightarrow 1$.

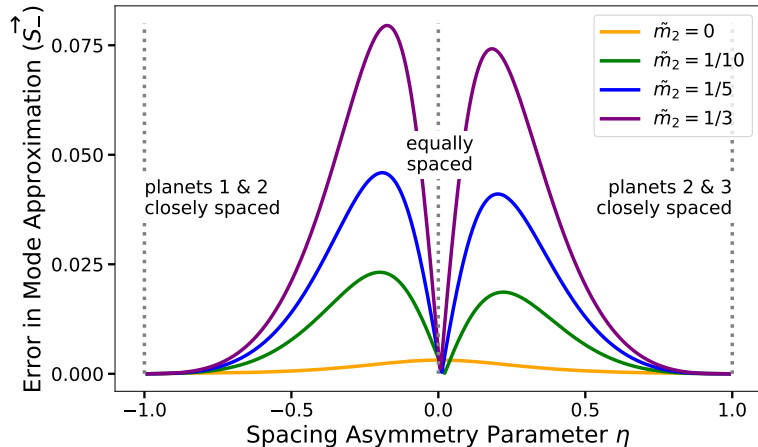


Figure 3.5: Error for our low-mass approximation of the \mathbf{e}_- eigenmode (Eq. 3.29) as we increase the mass of the middle planet from the test-particle case (orange curve) to the equal-mass case (purple curve). To isolate only errors in our low-mass approximation, we set $\alpha_{13} = 0.99$ so that the errors introduced by the compact approximation are negligible (Fig. 3.4). We plot the error as a function of the spacing asymmetry parameter η , so the left of the plot corresponds to placing the middle planet right next to its inner neighbor (and vice versa on the right of the plot), while $\eta = 0$ corresponds to uniform spacing.

We conclude that the low-mass result (Eq. 3.29) provides not only a simple expression, but also one with the correct asymptotic behavior of approaching \mathbf{e}_{12} (or \mathbf{e}_{23}) when the middle planet is very close to its inner (or outer) neighbor. However, it is worth noting that $\mathbf{S}_+ \propto \mathbf{e}_{13}$ does not have the correct asymptotic behavior. As we increase the mass of the middle planet, \mathbf{S}_+ is the correct eigen-mode for $\eta = 0$, but the error gets as large as 50% at large separation asymmetry for three equally massive planets.

The behavior when there are errors both due to wider separations and a massive middle planet is more complicated, since the errors can add or partially cancel in a variety of ways. To illustrate this, we remake Fig. 3.5 for a wider total spacing $\alpha_{13} = 0.78$. We see that the error pattern in Fig. 3.6 becomes skewed, and even the test-particle case has errors due to the wider separations.

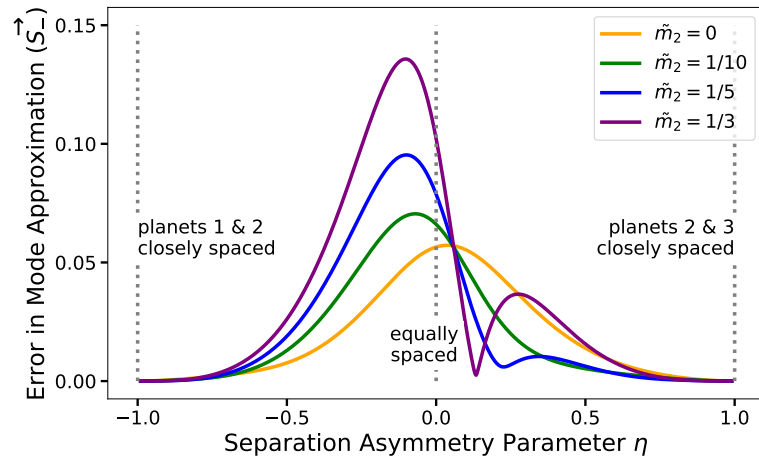


Figure 3.6: We loosen the compact limit constraint by remaking Fig. 3.5 with a more widely spaced $\alpha_{13} = 0.78$. The errors are now due both to wider spacings and a massive middle planet, leading to a more complicated pattern skewed towards negative η , and with non-zero error even in the test-particle case.

3.4.4 An Application

Finally, we compare these results directly against N-body integration. We consider two Earth-mass planets with period ratio 1.54, wide of the 3:2. We then insert an additional test particle with $\eta = -0.12$, corresponding to approximately uniform spacing. In the top panel of Fig. 3.7 we plot the variations of the magnitudes of e_{12} and e_{23} vs. time. We see that they are out of phase with one another, which is a generic result of the low-mass limit due to the opposite signs of e_- in the relative eccentricities in Eq. 3.31. This is reflected geometrically in the opposite directions of the green vectors in the two bottom left panels for the relative eccentricities in Fig. 3.3, corresponding to the same planetary system.

In the middle two panels of Fig. 3.7 we plot the time evolution of the three numerically calculated eigenmodes along with our approximated modes as a fractional deviation from their means, i.e., $[S(t) - \bar{S}]/\bar{S}$, where the bars denote mean values. If the Laplace-Lagrange approximation were exact, the lines in the second panel would be flat. Several effects could be responsible for the remaining variations, including higher-order secular terms ($\mathcal{O}(e^4)$), or nearby mean motion resonances (MMRs). One can average over the effects of nearby first-order MMRs, which modify the traditional Laplace-Lagrange matrix by introducing corrections in the entries at second order in the masses. We added these corrections using the `celmech` package to numerically obtain corrected eigenmodes—this reduced the fast “noise” on timescales of thousands of orbital periods, but does not eliminate longer-term variations on timescales of $\sim 10^4$ orbital periods. We therefore suspect the remaining variations to be due to other resonances we were unable to identify.

This numerically calculated second panel thus provides the best-case scenario that our approximated eigenmodes can hope to reproduce in the Laplace-Lagrange approximation. We see that the variations in our approximated modes in the third panel are approximately twice as large as the numerical ones in the second panel.

In the bottom panel we plot the errors in our approximated modes as their distances from the numerical ones, normalized by the mean magnitudes of the numerical modes, i.e., $|S_{app}(t) - S_{num}(t)|/\bar{S}_{num}$. We see that this removes the high-frequency “noise” (from terms not included in the Laplace-Lagrange approximation), and that the remaining error in S_- is $\lesssim 10\%$, while the errors in the remaining modes are significantly smaller.

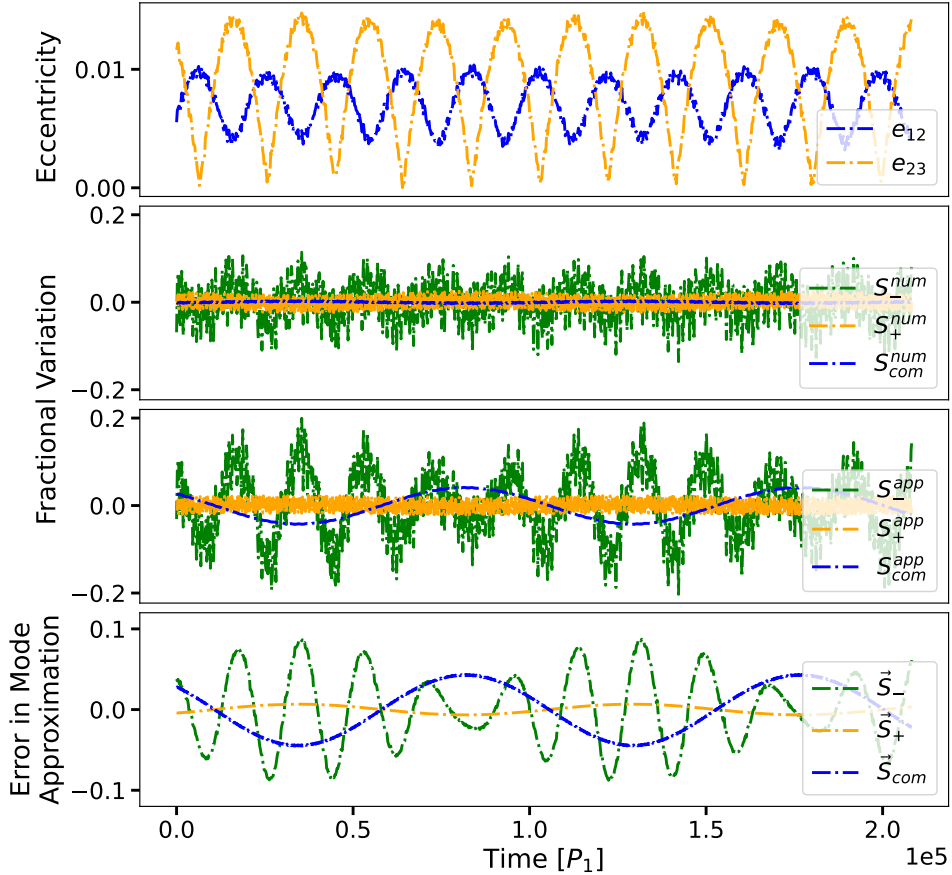


Figure 3.7: We consider a pair of Earth-mass planets with period ratio 1.54 wide of the 3:2 MMR, with a test particle placed approximately in the middle ($\eta = -0.12$). The eccentricities and pericenters are drawn to match the mode amplitudes and evolution depicted in Fig. 3.3). Top panel plots the relative eccentricities vs time. In the second panel we plot the relative variations of the numerical modes vs time, which would ideally remain at zero, and in the third panel we plot the approximated modes in Eq. 3.27 against time. Bottom panel plots the errors (as defined in the text) in our approximated modes from the numerical modes. We see that the errors remain $\lesssim 10\%$.

3.4.5 Summary

So far we have built up analytical model for the secular dynamics in compact three-planet systems. We began with considering the limit where the middle planet is much less massive than its neighbors. In this case, we could exploit the two-planet solution to identify two of the three eigenmodes of the system. We then obtained a general expression for the third eigenmode \mathbf{e}_- , in terms of dimensionless interaction strengths between the inner planet pair $\tilde{\chi}_{12}$ and the outer planet pair $\tilde{\chi}_{23}$ (Eq. 3.29). We showed that the individual and relative eccentricities can be represented by the vector sum of eigenmodes that precess at their own frequencies (Fig. 3.3, Eqs. 3.30-3.31). Finally, we explored how the limiting expression for \mathbf{e}_- performed as we relaxed our assumptions, i.e., increasing the mass of the middle planet and separating the orbits.

As mentioned in Ch. 2.2, secular variations in relative eccentricities cause the MMR widths to expand and contract, which could have significant impact on the stability boundary. In this chapter, we have obtained analytical expressions for the secular evolution of relative eccentricities in terms of the eigenmodes (Eq. 3.31). In the next chapter, we use these results to formulate a modified stability boundary under the secular effect.

Chapter 4

Modulation of the Stability Boundary

In the resonance overlap criterion, the boundary for widespread chaos between a pair of closely spaced planets is at the location where adjacent MMRs start overlapping. The width of each MMR is dependent on the relative eccentricity between the two planets. Hadden & Lithwick (2018) predicts that the relative eccentricity (e_{12} , Ch.2.3) above which the system becomes unstable (red line in Fig. 1.1) is given by

$$\tilde{e}_{12} \equiv \frac{e_{12}}{e_{c,12}} \approx C_1 \exp \left\{ -C_2 (m_1 + m_2)^{1/3} \left(\frac{a_2}{a_2 - a_1} \right)^{4/3} \right\}, \quad (4.1)$$

where $e_{c,12} \equiv 1 - a_1/a_2$ is the orbit-crossing eccentricity, m_i is the planet's mass relative to that of the star, and C_i is some positive fit parameter. Since \mathbf{e}_{12} is an eigenmode for a compact two-planet system, e_{12} is conserved and the stability boundary is fixed. As we add a perturbing third planet, however, secular modulation will drive oscillations in the relative eccentricities, and we need to consider the maximum value $e_{12,\max}$ in a secular cycle (Fig. 1.3).

In Sec. 3.4, we showed that the relative eccentricity vectors can be expressed as a linear combination of the conserved Laplace-Lagrange eigenmodes driving the dynamics:

$$\begin{pmatrix} \mathbf{e}_{12} \\ \mathbf{e}_{23} \end{pmatrix} = \begin{pmatrix} \tilde{\chi}_{23} \mathbf{e}_{13} - \mathbf{e}_- \\ \tilde{\chi}_{12} \mathbf{e}_{13} + \mathbf{e}_- \end{pmatrix}. \quad (4.2)$$

We can rewrite the three eigenmodes as

$$\begin{pmatrix} \mathbf{e}_- \\ \mathbf{e}_{13} \\ \mathbf{e}_{com} \end{pmatrix} = \begin{pmatrix} e_- \exp\{i(\omega_- t + \phi_-)\} \\ e_{13} \exp\{i(\omega_{13} t + \phi_{13})\} \\ e_{com} \exp\{i\phi_{com}\} \end{pmatrix}, \quad (4.3)$$

where the eigenfrequencies ω_i are given by Eqs. C.5-C.6, and ϕ_i are the initial phases of the modes. Then the magnitudes of the relative eccentricity vectors

that determine the MMR widths evolve as

$$e_{12}^2(t) = e_-^2 + \tilde{\chi}_{23}^2 e_{13}^2 - 2\tilde{\chi}_{23} e_- e_{13} \cos \theta(t), \quad (4.4)$$

$$e_{23}^2(t) = e_-^2 + \tilde{\chi}_{12}^2 e_{13}^2 + 2\tilde{\chi}_{12} e_- e_{13} \cos \theta(t), \quad (4.5)$$

where

$$\theta(t) = (\omega_- - \omega_{13})t + (\phi_- - \phi_{13}). \quad (4.6)$$

Since $\tilde{\chi}_{12}$ and $\tilde{\chi}_{23}$ are non-negative, there is always a π -phase difference in the evolution of e_{12} and e_{23} - when one resonance width expands, the other contracts. The maximum extents of expansion in the relative eccentricities are

$$\frac{e_{12,\max}}{e_{12}(0)} = \frac{e_- + \tilde{\chi}_{23} e_{13}}{\sqrt{e_-^2 + \tilde{\chi}_{23}^2 e_{13}^2 - 2\tilde{\chi}_{23} e_- e_{13} \cos(\phi_- - \phi_{13})}}, \quad (4.7)$$

$$\frac{e_{23,\max}}{e_{23}(0)} = \frac{e_- + \tilde{\chi}_{12} e_{13}}{\sqrt{e_-^2 + \tilde{\chi}_{12}^2 e_{13}^2 + 2\tilde{\chi}_{12} e_- e_{13} \cos(\phi_- - \phi_{13})}}. \quad (4.8)$$

In Appendix D, we discuss a method to minimize (denoted with superscript “off”) and maximize (denoted with superscript “on”) the amplitude of oscillations in e_{12} , under the constraint that both cases start at the same initial relative eccentricities ($e_{12}^{\text{off}} = e_{12}^{\text{on}}(0)$, $e_{23}^{\text{off}} = e_{23}^{\text{on}}(0)$). In the “off” scenario, there is no oscillation in the relative eccentricities. This allows us to elegantly explore the full range of possible behaviors, from negligible to maximum modification of the stability boundary by the secular dynamics.

In the “on” scenario, we show that the maximum extent of expansion in e_{12} is given by

$$\frac{e_{12,\max}^{\text{on}}}{e_{12}^{\text{on}}(0)} = \frac{e_{12,\max}^{\text{on}}}{e_{12}^{\text{off}}} = \frac{1}{\sqrt{\tilde{\chi}_{12}}} \quad (4.9)$$

when the inner pair is more strongly interacting, i.e., $\tilde{\chi}_{12} > \tilde{\chi}_{23}$. So the stability boundary as we maximize the secular modulation of e_{12} should be lower by a factor of $1/\sqrt{\tilde{\chi}_{12}}$ than the static boundary in Eq. 4.1:

$$\tilde{e}_{12}(0) \approx C_1 \sqrt{\tilde{\chi}_{12}} \exp \left\{ -C_2 (m_1 + m_2)^{1/3} \left(\frac{a_2}{a_2 - a_1} \right)^{4/3} \right\}. \quad (4.10)$$

Note that $\tilde{\chi}_{12}$ is dependent on a_1 and a_2 .

To compare the above results with simulation, we consider a hierarchical three-planet configuration where the inner two planets are tightly packed. The inner planet has a mass of $4 \times 10^{-5} M_\star$ (approximately 13 Earth masses) and is always placed at an orbital period $P_1 = 1$ yr. We vary the period of the massless middle planet P_2 from the 4:3 MMR to the 3:2 MMR with the inner planet. To avoid being in MMRs with the third planet, we place the latter at a period

$P_3 = 3.2$ yr that is far away from low-order resonances. In order for the perturbing third planet to induce substantial secular modulation, we assign it a mass of $8 \times 10^{-4} M_\star$, or slightly less than the mass of Jupiter relative to the Sun.

We vary the period of the middle planet P_2 along one axis and the initial value of \tilde{e}_{12} along the other axis. For each configuration we run a numerical integration over the secular timescale using the WHFast integrator in the REBOUND N-body package. We then measure the Mean Exponential Growth of Nearby Orbits (MEGNO) (Cincotta et al., 2003) as a chaos indicator.

We plot the results in Fig. 4.1 for two different scenarios: when we introduce no secular effect (i.e., “turn off” oscillations in e_{12}) and when we maximize the secular effect (i.e., “turn on” oscillations in e_{12}). The yellow regions are chaotic, while the dark-green regions are stable. The solid black lines represent the maximum widths of all MMRs up to 10th order between the compact inner pair of planets, which are constant when there is no secular effect.¹ The dashed blue lines show the MMRs between the middle and the outer planet, which have negligible widths. Widespread chaos takes place once the MMRs start overlapping.² The purple line in the top panel fits the locations of resonance overlap to the analytical stability boundary in Eq. 4.1. The bottom panel plots the modulated stability boundary according to Eq. 4.10, using the same fit parameters as above. We see that the maximum modulation of the chaotic boundary predicted by Eq. 4.10 agrees with the simulated results. Around the 3:2 MMR, the modulation can be as large as $\sim 40\%$.

As we proceed from this hierarchical case, where the inner planet pair is significantly more compact, contributions from other dynamical mechanisms, such as the three-body MMRs, will become important. We hope that the analytical framework we developed will be useful in disentangling the contributions from other sources of chaos in the future.

¹The resonance widths are given by $\frac{\delta P}{P} \approx \frac{3}{2} \frac{\delta a}{a}$, where the half-width δa of a k th-order MMR is $\frac{\delta a}{a} \approx 4\sqrt{\frac{h_k}{3}} (m_1 + m_2)^{1/2} \tilde{e}_{12}^{k/2}$, and h_k is a constant specific to each set of k th-order MMRs (Hadden & Lithwick, 2018).

²Additionally there are chaotic regions around the boundary of each resonance due to perturbations from three-body MMRs, which is discussed in Appendix A.

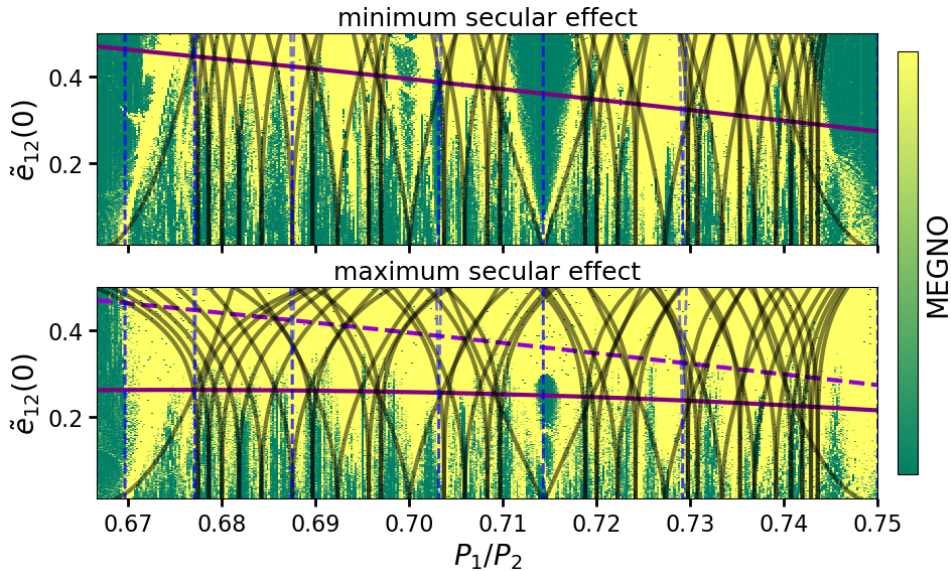


Figure 4.1: Secular evolution can strongly modulate the stability boundary. In the top panel where there is no secular variation in e_{12} , the system has a fixed stability boundary. The black lines show the MMRs between the inner planet pair. The stability boundary in purple is a linear fit to Eq. 4.1 based on where MMRs start to overlap, and the fit parameters are $C_1 = 1.4$ and $C_2 = 4.6$. Secular perturbations push the stability boundary downward. The bottom panel plots the maximum MMR widths in black. The solid purple line shows the lower bound of the stability boundary predicted by Eq. 4.10 using the same fit parameters. The dashed line duplicates the boundary without secular effect above, which is also the upper bound of the stability boundary. When the middle planet is close to 3:2 MMR with the inner planet, the secular modulation of the stability boundary can be as large as $\sim 40\%$. In general, the extent of this modulation is dependent on a specific combination of planet's mass and spacing, which is specified in Eqs. 3.29 and 4.9.

Chapter 5

Conclusion

The criterion for widespread chaos in compact two-planet systems is set by the boundary where adjacent mean motion resonances start to overlap one another (Fig. 1.1). Most planetary systems have more than two planets, and in this case two new dynamical effects drive chaos: three-body resonances (Rath et al., 2022) and slow expansion and contraction of the MMR widths due to long-term “secular” oscillations in the orbital eccentricities (Tamayo et al., 2021b). While analytical theory for the former mechanism was previously developed (Rath et al., 2022), the latter had only been explored numerically.

The goal of this thesis was thus to develop closed-form expressions for the maximum widths of MMRs under secular evolution and the resultant change in the stability boundary. This elucidates the key combinations among the many system parameters that dominantly determine the stability of a given planetary system, and provides an analytical framework that can be used in the future to disentangle the relative importance of 3-body resonances vs. secular evolution in different regimes.

We showed that in the limit where the orbits are closely spaced, the numerically derived Laplace-Lagrange eigenmodes driving the secular dynamics simplify to easily understood expressions in terms of the combinations of eccentricities that set the MMR widths. We built on previous intuition that a general result for N tightly spaced orbits is that in the compact limit, the center-of-mass eccentricity vector $\mathbf{e}_{com} = \sum_{i=1}^N \tilde{m}_i \mathbf{e}_i$ is always conserved (Goldreich & Tremaine, 1981). This implies that this linear combination of the eccentricities must correspond to one of the N conserved Laplace-Lagrange eigenmodes in an N -planet system, with zero associated eigenfrequency. Additionally, Tamayo et al. (2021b) showed that in the two-planet case, the remaining eigenmode corresponds to the relative eccentricity vector $\mathbf{e}_{12} = \mathbf{e}_2 - \mathbf{e}_1$, which rotates at constant magnitude and is the same combination of eccentricities that sets the widths of MMRs in the general case of two eccentric orbits (Ch.2.3). This has the important implication that in the two-planet case, the widths of MMRs are fixed in time, and

thus Fig. 1.1 and the associated stability boundary remain static.

We built up the three-planet case in Chapter 3 by first considering the limit where the middle planet is much less massive than its neighbors. In this setup, the two massive planets are unaffected by the third body and thus follow two-planet dynamics, so we could exploit the above understanding of the two-planet solution to identify two of the three eigenmodes of the system. We could then determine the third eigenvector from the requirement that the transformation between the original eccentricities and the system's eigenmodes correspond to a rotation. We parametrized our general expression for the third mode e_- , in terms of dimensionless interaction strengths between the inner pair of planets $\tilde{\chi}_{12}$ and the outer pair of planets $\tilde{\chi}_{23}$ (Eq. 3.29). Finally, we explored how this limiting expression for e_- performed as we relaxed our assumptions, increasing the mass of the middle planet and separating the orbits. We found that even going out to period ratios of 3:2 between adjacent planets, the error in the mode remained $\lesssim 10\%$ (Fig. 3.4). Additionally, varying the middle planet's mass from a test particle to the equal-mass case, the error also remains below 10% (Fig. 3.5).

This provides a simple interpretation for a geometric picture in which the individual or relative eccentricities are the vector sum of contributions from each of the eigenmodes that each precess at their own rates (Fig. 3.3, Eqs. 3.30–3.31). These results have a wide range of applications beyond the particular question of orbital stability, since the secular modes of observed planetary systems (previously studied numerically) is thought to encode information about its formation (Van Laerhoven & Greenberg, 2012) and evolution under tidal interactions with the host star (Greenberg & Van Laerhoven, 2011), and resonances between the eigenfrequencies of these secular modes is a separate mechanism for driving chaos and forming planets in tight orbits around their host stars (Petrovich et al., 2019).

Finally, in Chapter 4 and Appendix D, we used these results to both calculate the extent of expansion of MMR widths (Eqs. 4.7–4.8), as well as how far down this effect drives the stability boundary in Fig. 4.1 (i.e., the maximum initial relative eccentricity for the system to stay stable). We derived both general expressions, as well as simple upper limits for how much the secular effect adding secular perturbation can modify the stability boundary (solid vs dashed lines in the bottom panel of Fig. 4.1). Both depend on the particular system configuration, but for the latter we show that the critical eccentricity on the stability boundary changes simply by a factor of $\sqrt{\tilde{\chi}_{12}}$ (Eq. D.9) for the inner planet pair, and by $\sqrt{\tilde{\chi}_{23}}$ (Eq. D.12) for the outer pair.

As discussed in the introduction, these results should be valuable to field both in the broad goal of connecting disk formation models to the mature exoplanet sample, and for stability constrained characterization of new exoplanet system discoveries. In addition to these applications, we hope these results can provide an analytic framework for disentangling the competing effects of the

secular dynamics studied here, and of three-body resonances investigated by Rath et al. (2022). Understanding the specific combinations of masses and orbital parameters that drive the secular evolution should enable the development of controlled numerical experiments to isolate secular effects from three-body MMR effects, thereby identifying the dominant drivers of chaos in different regimes observed across the exoplanet sample.

Acknowledgements

I would like to express my deepest gratitude to my thesis advisor Daniel Tamayo. This work would not have been possible without his physical insight into the problem and his endless support during the semesters. I am indebted to him for the sleep he sacrificed and for the croissants from Crème Bakery he kindly shared after I pulled all-nighters. I would also like to thank Yoram Lithwick, Scott Tremaine and an anonymous reviewer for giving constructive feedback on the secular dynamics model, and all the group members from the Planetary Origin and Evolution Lab for their useful suggestions along my research. Lastly, I would like to mention Rosy Chen for the wonderful and deadly hikes we did together to set off the semester, Jolyne Lin for being the best listener and boba buddy, and Lucien Tsai for the entertainment he brought along the way.

Appendix A

Three-body MMRs

In a three-planet system, the presence of chaos is generally due to the 2-body MMR overlap, similar to the two-planet scenario (Tamayo et al., 2021b). However, this criterion only agrees with numerical simulations at a crude level, and greater accuracy is attained by considering chaotic regions around neighboring MMRs that do not overlap (Rath et al., 2022).

To see how the latter criterion is applied, we reduce the middle planet to a test particle and examine its motion under the perturbation by two MMRs - one $j_1 : j_1 - k_1$ resonance from the inner planet (denoted with subscript 1) and one $j_2 : j_2 + k_2$ resonance from the outer planet (denoted with subscript 2). Rath et al. (2022) model such system as a perturbed pendulum with Hamiltonian

$$\mathcal{H} = \frac{1}{2}\dot{\phi}^2 - \epsilon_1 \cos \phi - \epsilon_2 \cos(r(\phi - vt)), \quad (\text{A.1})$$

where ϕ is the longitude of conjunction angle when the test particle is at resonance with the inner planet, ϵ_i is proportional to the planet's mass and the relative eccentricity to the test particle, r is the integer ratio j_2/j_1 , and v a parameter that quantifies the separation in phase space between the two resonances (see the orange arrows in Fig. A.1).

In Fig. A.1, we plot the phase space diagram (or “surface of section”) of the three-planet system described by Eq. A.1.¹ We end up with two cat’s eyes stacked along the y-axis. As we decrease the value of v , i.e., decreasing the separation between two resonances, the cat’s eyes start merging and the chaotic regions around the separatrices expand.

We combine the results for all values of v by taking a “double surface of section”: we take a cross section in each phase space plot at $\phi = 0$ and recording the values of ϕ where the trajectories are chaotic. The result is shown in Fig. A.2,

¹For each integrated trajectory, we plot snapshots at $rvt = 2k\pi$, where k is a non-negative integer. Stable trajectories will create 1D curves in the $\phi-\dot{\phi}$ plane, while chaotic ones will randomly fill a 2D region (Rath et al., 2022).

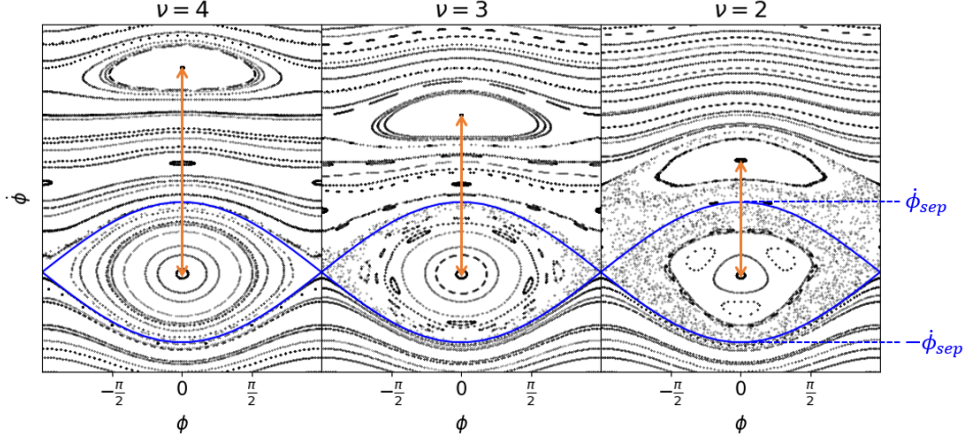


Figure A.1: Phase space plots of a three-planet system modeled by Eq. A.1. The value of v describes the separation between the two resonances, which is equal to the length of the orange arrow. The chaotic zones (random dots) around the separatrices expand as the resonances become closer to each other.

where the chaotic regions are marked in black. Rath et al. (2022) derived an analytical expression for the width of the chaotic zones, which we will discuss in detail in Ch. 4. Qualitatively speaking, the width of the chaotic regions peaks around $v \sim \mathcal{O}(1)$ (i.e., when there is large overlap of MMRs) and decays exponentially as v increases (i.e., when the resonances have wider separation).

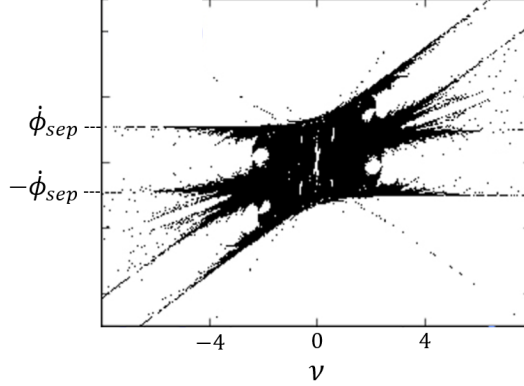


Figure A.2: Double surface of section, adapted from (Rath et al., 2022). We plot the chaotic regions around the separatrix in black at different values of v .

We can map the pendulum parameters $\{r, v, \epsilon_1, \epsilon_2, \phi, \dot{\phi}\}$ to the orbital elements $\{m_1, m_2, P_1, P_2, \lambda, a\}$. This allows us to extend the double surfaces of sec-

tion in Fig. A.2 to a global stability plot in terms of period ratios. We fix the orbital period of the test particle P while varying the period of the inner planet P_1 and the outer planet P_2 . We show an example of the resulting stability plot in Fig. A.3. Left panel shows the locations and widths of two-body MMRs between the inner pair (vertical blue bands) and the outer pair of planets (horizontal blue bands). The overlapping zones are marked in red. Right panel plots the predicted regions where chaos should occur, each of which has the shape of the double surface of section.

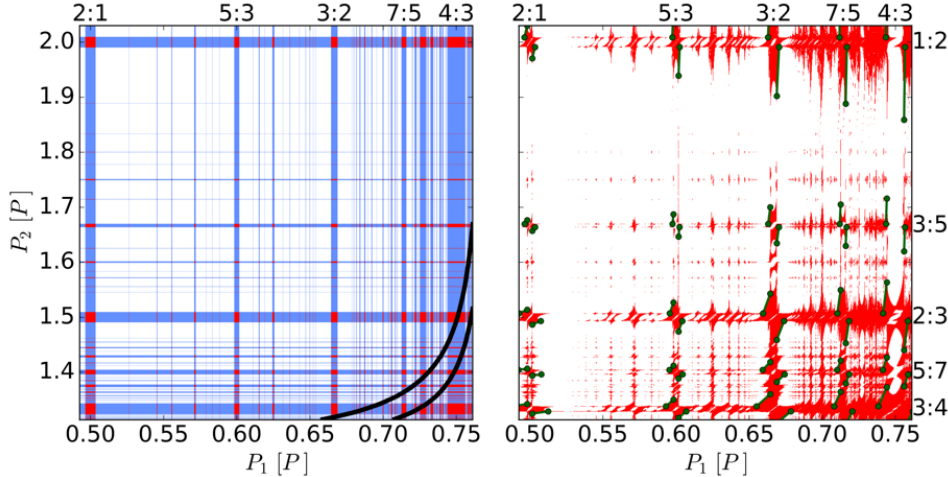


Figure A.3: Chaotic regions due to overlap of two-body MMRs from each pair, copied from (Rath et al., 2022). As we move to the right along the x-axis, we obtain configurations with closer separations between the test particle and its inner neighbor, and as we move down along the y-axis, the test particle is initialized closer to its outer neighbor. Left panel shows the locations and widths of two-body MMRs between the inner two planets in vertical blue bands and the ones between the outer two planets in horizontal blue bands. The overlapping zones are red. Right panel shows the predicted chaotic regions based on double surface of section.

Appendix B

Laplace-Lagrange Hamiltonian

Expressed in terms of orbital elements, the Hamiltonian \mathcal{H} for a three-planet system is

$$\mathcal{H} = -\frac{Gm_1m_2}{a_2}\mathcal{R}_{sec,12} - \frac{Gm_2m_3}{a_3}\mathcal{R}_{sec,23} - \frac{Gm_1m_3}{a_3}\mathcal{R}_{sec,13}, \quad (\text{B.1})$$

where, to the leading order in eccentricities, the secular disturbing functions between a pair of planets is (Murray & Dermott, 2000),

$$R_{sec,ij} = \frac{\alpha_{ij}}{8} \left[b_{3/2}^{(1)}(\alpha_{ij})(e_i^2 + e_j^2) - 2b_{3/2}^{(2)}(\alpha_{ij})e_i e_j \cos(\omega_j - \omega_i) \right], \quad (\text{B.2})$$

the $\alpha_{ij} \equiv a_i/a_j$ are the semimajor axis ratios, and $b_s^{(m)}$ are Laplace coefficients evaluated at α_{ij} . While in our final expressions we will approximate the $\alpha_{ij} \approx 1$ in the compact limit, we retain them in this Appendix for reference. These disturbing functions can be written in matrix notation and in terms of complex eccentricities (Eq. 3.4) as

$$R_{sec,ij} = \frac{\alpha_{ij}}{8} \begin{pmatrix} \mathbf{e}_i^* & \mathbf{e}_j^* \end{pmatrix} \begin{pmatrix} b_{3/2}^{(1)}(\alpha_{ij}) & -b_{3/2}^{(2)}(\alpha_{ij}) \\ -b_{3/2}^{(2)}(\alpha_{ij}) & b_{3/2}^{(1)}(\alpha_{ij}) \end{pmatrix} \begin{pmatrix} \mathbf{e}_i \\ \mathbf{e}_j \end{pmatrix}. \quad (\text{B.3})$$

Our goal is to write the Hamiltonian in terms of the canonical complex \mathbf{G}_i variables. If we just take the terms for the outermost pair of planets, rewriting the prefactor and taking $\mathbf{e}_i^* = \mathbf{G}_i/\sqrt{\Lambda_i}$, we have

$$\begin{aligned} \mathcal{H}_{23} &= -\frac{\Lambda_2\Lambda_3\alpha_{23}}{8a_3M_\star\sqrt{a_2a_3}} \begin{pmatrix} \mathbf{G}_2 & \mathbf{G}_3 \end{pmatrix} \begin{pmatrix} b_{3/2}^{(1)}(\alpha_{23}) & -b_{3/2}^{(2)}(\alpha_{23}) \\ -b_{3/2}^{(2)}(\alpha_{23}) & b_{3/2}^{(1)}(\alpha_{23}) \end{pmatrix} \begin{pmatrix} \frac{\mathbf{G}_2^*}{\sqrt{\Lambda_2}} \\ \frac{\mathbf{G}_3^*}{\sqrt{\Lambda_3}} \end{pmatrix} \\ &= -\sqrt{\frac{GM_\star}{a_3^3}} \frac{1}{8M_\star} (\mathbf{G}_1 \quad \mathbf{G}_2 \quad \mathbf{G}_3) \begin{pmatrix} 0 & 0 & 0 \\ 0 & b_{3/2}^{(1)}(\alpha_{23})\alpha_{23}^{1/2}m_3 & -b_{3/2}^{(2)}(\alpha_{23})\alpha_{23}^{3/4}\sqrt{m_2m_3} \\ 0 & -b_{3/2}^{(2)}(\alpha_{23})\alpha_{23}^{3/4}\sqrt{m_2m_3} & b_{3/2}^{(1)}(\alpha_{23})\alpha_{23}m_2 \end{pmatrix} \begin{pmatrix} \mathbf{G}_1^* \\ \mathbf{G}_2^* \\ \mathbf{G}_3^* \end{pmatrix}, \end{aligned} \quad (\text{B.4})$$

where in the second equality we additionally expand our matrices to include \mathbf{G}_1 (with corresponding zero entries) to make it easier to combine this expression with the corresponding \mathcal{H}_{ij} for the other two pairs of planets. The contributions \mathcal{H}_{23} and \mathcal{H}_{13} can be easily found by relabeling the inner and outer planets using Eq. B.4 and shifting the entries in the large middle matrix to pick out the appropriate \mathbf{G}_i ; however, while \mathcal{H}_{13} shares the same prefactor proportional to the outer body's mean motion $n_3 = \sqrt{GM_\star/a_3^3}$, $\mathcal{H}_{12} \propto n_2 = n_3 \alpha_{23}^{-3/2}$. If we choose to pull out a common factor n_3 from all pairs, and additionally introduce masses scaled by the total planetary mass, $\tilde{m}_i \equiv m_i/m_{tot}$, we finally obtain

$$\mathcal{H} = -\frac{1}{2} (\mathbf{G}_1 \quad \mathbf{G}_2 \quad \mathbf{G}_3) \cdot \mathcal{M} \cdot \begin{pmatrix} \mathbf{G}_1^* \\ \mathbf{G}_2^* \\ \mathbf{G}_3^* \end{pmatrix}, \quad (\text{B.5})$$

where

$$\mathcal{M} = \frac{n_3}{4} \frac{m_{tot}}{M_\star} \begin{pmatrix} x_{11} & x_{12} & x_{13} \\ x_{12} & x_{22} & x_{23} \\ x_{13} & x_{23} & x_{33} \end{pmatrix}, \quad (\text{B.6})$$

where

$$\begin{aligned} x_{11} &= \alpha_{12}^{1/2} \alpha_{23}^{-3/2} b_{3/2}^{(1)}(\alpha_{12}) \tilde{m}_2 + \alpha_{13}^{1/2} b_{3/2}^{(1)}(\alpha_{13}) \tilde{m}_3, \\ x_{12} &= -\alpha_{12}^{3/4} \alpha_{23}^{-3/2} b_{3/2}^{(2)}(\alpha_{12}) \sqrt{\tilde{m}_1 \tilde{m}_2} \\ x_{13} &= -\alpha_{13}^{3/4} b_{3/2}^{(2)}(\alpha_{13}) \sqrt{\tilde{m}_1 \tilde{m}_3} \\ x_{22} &= \alpha_{12} \alpha_{23}^{-3/2} b_{3/2}^{(1)}(\alpha_{12}) \tilde{m}_1 + \alpha_{23}^{1/2} b_{3/2}^{(1)}(\alpha_{23}) \tilde{m}_3 \\ x_{23} &= -\alpha_{23}^{3/4} b_{3/2}^{(2)}(\alpha_{23}) \sqrt{\tilde{m}_2 \tilde{m}_3}, \\ x_{33} &= \alpha_{13} b_{3/2}^{(1)}(\alpha_{13}) \tilde{m}_1 + \alpha_{23} b_{3/2}^{(1)}(\alpha_{23}) \tilde{m}_2 \end{aligned} \quad (\text{B.7})$$

Appendix C

Approximated Eigenvalues

The rotated Laplace-Lagrange matrix given in Eq. 3.17 is

$$\mathcal{M}' = \begin{pmatrix} \omega'_1 & k & 0 \\ k & \omega'_2 & 0 \\ 0 & 0 & 0 \end{pmatrix} + \delta\omega'_1 \mathcal{M}_d, \quad (\text{C.1})$$

where δ drops to zero in the compact limit as we show in Fig. C.1. The non-zero elements remained in the matrix are

$$\begin{aligned} \omega'_1 = \frac{n_3}{4} \frac{m_{tot}}{M_\star} \left\{ \frac{\tilde{m}_1}{\tilde{m}_1 + \tilde{m}_3} \alpha_{12}^{1/2} \alpha_{23}^{-3/2} \left[\tilde{m}_2^2 b_{3/2}^{(1)}(\alpha_{12}) + (\tilde{m}_1 + \tilde{m}_3)^2 \alpha_{12}^{1/2} b_{3/2}^{(1)}(\alpha_{12}) + 2\tilde{m}_2(\tilde{m}_1 + \tilde{m}_3) \alpha_{12}^{1/4} b_{3/2}^{(2)}(\alpha_{12}) \right] \right. \\ \left. + \frac{\tilde{m}_3}{\tilde{m}_1 + \tilde{m}_3} \alpha_{23} \left[\tilde{m}_2^2 b_{3/2}^{(1)}(\alpha_{23}) + (\tilde{m}_1 + \tilde{m}_3)^2 \alpha_{23}^{-1/2} b_{3/2}^{(1)}(\alpha_{23}) + 2\tilde{m}_2(\tilde{m}_1 + \tilde{m}_3) \alpha_{23}^{-1/4} b_{3/2}^{(2)}(\alpha_{23}) \right] \right\}, \end{aligned} \quad (\text{C.2})$$

$$\begin{aligned} \omega'_2 = \frac{n_3}{4} \frac{m_{tot}}{M_\star} \left\{ \frac{\tilde{m}_2}{\tilde{m}_1 + \tilde{m}_3} \left(\tilde{m}_3 \alpha_{12}^{1/2} \alpha_{23}^{-3/2} b_{3/2}^{(1)}(\alpha_{12}) + \tilde{m}_1 \alpha_{23} b_{3/2}^{(1)}(\alpha_{23}) \right) \right. \\ \left. + \frac{1}{\tilde{m}_1 + \tilde{m}_3} \alpha_{13} \left(\tilde{m}_1^2 b_{3/2}^{(1)}(\alpha_{13}) + \tilde{m}_3^2 \alpha_{13}^{-1/2} b_{3/2}^{(1)}(\alpha_{13}) + 2\tilde{m}_1 \tilde{m}_3 \alpha_{13}^{-1/4} b_{3/2}^{(2)}(\alpha_{13}) \right) \right\}, \end{aligned} \quad (\text{C.3})$$

$$\begin{aligned} k = \frac{n_3}{4} \frac{m_{tot}}{M_\star} \frac{\sqrt{\tilde{m}_1 \tilde{m}_2 \tilde{m}_3}}{\tilde{m}_1 + \tilde{m}_3} \left\{ \alpha_{23} \left[\tilde{m}_2 b_{3/2}^{(1)}(\alpha_{23}) + (\tilde{m}_1 + \tilde{m}_3) \alpha_{23}^{-1/4} b_{3/2}^{(2)}(\alpha_{23}) \right] \right. \\ \left. - \alpha_{12}^{1/2} \alpha_{23}^{-3/2} \left[\tilde{m}_2 b_{3/2}^{(1)}(\alpha_{12}) + (\tilde{m}_1 + \tilde{m}_3) \alpha_{12}^{1/4} b_{3/2}^{(2)}(\alpha_{12}) \right] \right\}. \end{aligned} \quad (\text{C.4})$$

If we assume that $b_{3/2}^{(1)}(\alpha_{ij}) = b_{3/2}^{(2)}(\alpha_{ij})$ and $\alpha_{ij}^{1/4} = 1$ in the square brackets in order to combine terms, the expressions reduce to

$$\omega'_1 = \frac{n_3}{2\pi} \frac{m_{tot}}{M_\star} \left(\frac{\tilde{m}_1}{\tilde{m}_1 + \tilde{m}_3} \frac{1}{e_{c,12}^2} + \frac{\tilde{m}_3}{\tilde{m}_1 + \tilde{m}_3} \frac{1}{e_{c,23}^2} \right), \quad (\text{C.5})$$

$$\omega'_2 = \frac{n_3}{2\pi} \frac{m_{tot}}{M_\star} \left[\tilde{m}_2 \left(\frac{\tilde{m}_3}{\tilde{m}_1 + \tilde{m}_3} \frac{1}{e_{c,12}^2} + \frac{\tilde{m}_1}{\tilde{m}_1 + \tilde{m}_3} \frac{1}{e_{c,23}^2} \right) + (\tilde{m}_1 + \tilde{m}_3) \frac{1}{e_{c,13}^2} \right], \quad (\text{C.6})$$

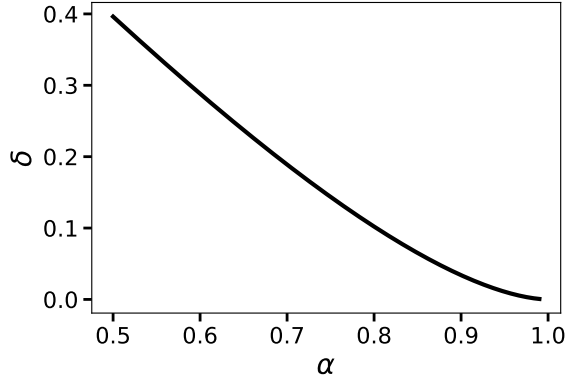


Figure C.1: The value of $\delta \equiv \left(b_{3/2}^{(1)}(\alpha) - b_{3/2}^{(2)}(\alpha) \right) / b_{3/2}^{(1)}(\alpha)$ as a function of α . The value of δ is $\lesssim 0.15$ for $\alpha > 0.75$ and drops to zero as α approaches unity.

$$k = \frac{n_3}{2\pi} \frac{m_{tot}}{M_\star} \frac{\sqrt{\tilde{m}_1 \tilde{m}_2 \tilde{m}_3}}{\tilde{m}_1 + \tilde{m}_3} \left(\frac{1}{e_{c,23}^2} - \frac{1}{e_{c,12}^2} \right), \quad (\text{C.7})$$

where

$$e_{c,12} \equiv \alpha_{12}^{-1/4} \alpha_{23}^{5/8} (1 - \alpha_{12}), \quad e_{c,23} \equiv \alpha_{12}^{1/8} \alpha_{23}^{-1/2} (1 - \alpha_{23}), \quad e_{c,13} \equiv \alpha_{13}^{-1/2} (1 - \alpha_{13}). \quad (\text{C.8})$$

While we retain these more accurate expressions for reference, for simplicity in the main text we set the α_{ij} prefactors in Eq. C.8 to unity in generating our plots as appropriate in the compact limit.

Appendix D

Extremizing the Secular Modulation

As stated in Eqs. 4.4 - 4.5, the relative eccentricities evolve as

$$e_{12}^2(t) = e_-^2 + \tilde{\chi}_{23}^2 e_{13}^2 - 2\tilde{\chi}_{23} e_- e_{13} \cos\{(\omega_- - \omega_{13})t + (\phi_- - \phi_{13})\}, \quad (\text{D.1})$$

$$e_{23}^2(t) = e_-^2 + \tilde{\chi}_{12}^2 e_{13}^2 + 2\tilde{\chi}_{12} e_- e_{13} \cos\{(\omega_- - \omega_{13})t + (\phi_- - \phi_{13})\}. \quad (\text{D.2})$$

We can minimize (denoted with superscript “off”) and maximize (denoted with superscript “on”) the oscillations in relative eccentricities by initializing the orbital elements accordingly.

We impose the constraint that both cases start at the same initial values:

$$e_{12}^{\text{off}} = e_{12}^{\text{on}}(0), \quad e_{23}^{\text{off}} = e_{23}^{\text{on}}(0). \quad (\text{D.3})$$

To minimize oscillations, we set $e_{13}^{\text{off}} = 0$ such that

$$e_{12}^{\text{off}} = e_{23}^{\text{off}} = e_-^{\text{off}}. \quad (\text{D.4})$$

Given the initial conditions in Eq. D.3, we then have

$$e_{13}^{\text{on}} = \left[\left(\frac{\tilde{\chi}_{23} - \tilde{\chi}_{12}}{2 \cos \phi_0} \right)^2 + \tilde{\chi}_{12} \tilde{\chi}_{23} \right]^{-1/2} e_{12}^{\text{off}}, \quad (\text{D.5})$$

$$e_-^{\text{on}} = \frac{\tilde{\chi}_{23} - \tilde{\chi}_{12}}{2 \cos \phi_0} \left[\left(\frac{\tilde{\chi}_{23} - \tilde{\chi}_{12}}{2 \cos \phi_0} \right)^2 + \tilde{\chi}_{12} \tilde{\chi}_{23} \right]^{-1/2} e_{12}^{\text{off}}, \quad (\text{D.6})$$

where $\phi_0 = \phi_- - \phi_{13}$ is the initial phase difference between the modes e_- and e_{13} . Following Ch. 4, we assume that the inner pair is more strongly interacting than the outer pair ($\tilde{\chi}_{12} > 1/2$) and maximize the quantity

$$\frac{e_{12,\text{max}}^{\text{on}}}{e_{12}^{\text{off}}} = \left(\tilde{\chi}_{23} + \frac{\tilde{\chi}_{23} - \tilde{\chi}_{12}}{2 \cos \phi_0} \right) \left[\left(\frac{\tilde{\chi}_{23} - \tilde{\chi}_{12}}{2 \cos \phi_0} \right)^2 + \tilde{\chi}_{12} \tilde{\chi}_{23} \right]^{-1/2} \quad (\text{D.7})$$

with respect to ϕ_0 . The solution is

$$\begin{cases} \phi_0 = \arccos\left(\frac{1-2\tilde{\chi}_{12}}{2\tilde{\chi}_{12}}\right), \\ e_{-}^{\text{on}} = \sqrt{\tilde{\chi}_{12}}e_{12}^{\text{off}}, \\ e_{13}^{\text{on}} = \frac{1}{\sqrt{\tilde{\chi}_{12}}}e_{12}^{\text{off}}. \end{cases} \quad (\text{D.8})$$

The corresponding extents of expansion in e_{12} and e_{23} relative to their initial values are

$$\frac{e_{12,\text{max}}^{\text{on}}}{e_{12}^{\text{on}}(0)} = \frac{1}{\sqrt{\tilde{\chi}_{12}}}, \quad \frac{e_{23,\text{max}}^{\text{on}}}{e_{23}^{\text{on}}(0)} = 2\sqrt{\tilde{\chi}_{12}}. \quad (\text{D.9})$$

When the inner pair interact significantly more strongly, they form a 2-planet “subsystem” where e_{12} becomes conserved. This matches with our prediction above that $e_{12,\text{max}}^{\text{on}}/e_{12}^{\text{on}}(0) \rightarrow 1$ for $\tilde{\chi}_{12} \rightarrow 1$. We can further relate the solution to the orbital elements through the following mapping:

$$\begin{pmatrix} \mathbf{e}_- \\ \mathbf{e}_{13} \\ \mathbf{e}_{\text{com}} \end{pmatrix} = \begin{pmatrix} \tilde{\chi}_{12} & -1 & \tilde{\chi}_{23} \\ -1 & 0 & 1 \\ \tilde{m}_1 & \tilde{m}_2 & \tilde{m}_3 \end{pmatrix} \cdot \begin{pmatrix} \mathbf{e}_1 \\ \mathbf{e}_2 \\ \mathbf{e}_3 \end{pmatrix}. \quad (\text{D.10})$$

In Fig. D.1, we show an example of how the relative eccentricities evolve as we minimize and maximize the secular modulation of e_{12} using the method described above.

Similarly, when the outer pair is more strongly interacting ($\tilde{\chi}_{23} > 1/2$), we can maximize the expansion in e_{23} by setting

$$\begin{cases} \phi_0 = -\frac{1-2\tilde{\chi}_{23}}{2\tilde{\chi}_{23}}, \\ e_{-}^{\text{on}} = \sqrt{\tilde{\chi}_{23}}e_{13}^{\text{off}}, \\ e_{13}^{\text{on}} = \frac{1}{\sqrt{\tilde{\chi}_{23}}}e_{13}^{\text{off}}. \end{cases} \quad (\text{D.11})$$

And the corresponding extents of expansions are

$$\frac{e_{12,\text{max}}^{\text{on}}}{e_{12}^{\text{on}}(0)} = 2\sqrt{\tilde{\chi}_{23}}, \quad \frac{e_{23,\text{max}}^{\text{on}}}{e_{23}^{\text{on}}(0)} = \frac{1}{\sqrt{\tilde{\chi}_{23}}}. \quad (\text{D.12})$$

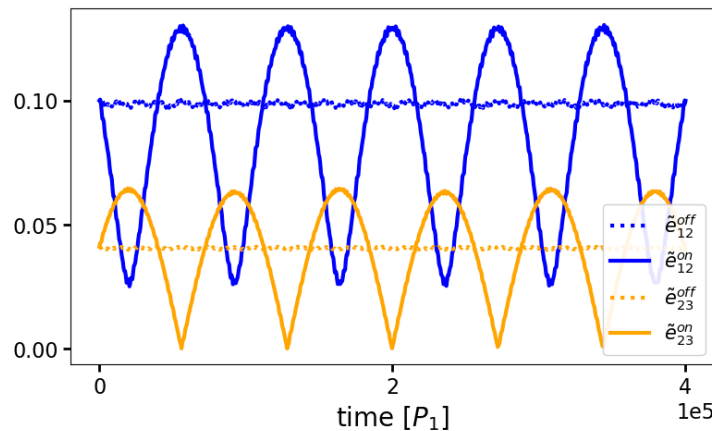


Figure D.1: The evolution of each normalized relative eccentricity ($\tilde{e}_{ij} \equiv e_{ij}/e_{c,ij}$) as we minimize and maximize the secular variations of e_{12} . The inner planet has a mass M_\oplus and an orbital period of 1 yr. We add a massless middle planet at $P_2 = 1.35$ yr, or equivalently, at $\alpha_{12} = 0.82$. A $20M_\oplus$ perturbing third planet is placed at $P_3 = 3.2$ yr to avoid MMRs with the inner pair. We initialize the orbital elements such that $\tilde{e}_{12}(0) = 0.1$. Under this configuration, the predicted extent of expansion in e_{12} relative to its initial value is $1/\sqrt{\tilde{\chi}_{12}} = 1.3$.

Bibliography

- Armitage, P. J. 2018, A Brief Overview of Planet Formation (Springer International Publishing), 2185–2203, doi: [10.1007/978-3-319-55333-7_135](https://doi.org/10.1007/978-3-319-55333-7_135)
- Arnol'd, V. I. 1963a, Russian Mathematical Surveys, 18, 9, doi: [10.1070/RM1963v018n05ABEH004130](https://doi.org/10.1070/RM1963v018n05ABEH004130)
- . 1963b, Russian Mathematical Surveys, 18, 85, doi: [10.1070/RM1963v018n06ABEH001143](https://doi.org/10.1070/RM1963v018n06ABEH001143)
- Chambers, J., Wetherill, G., & Boss, A. 1996, Icarus, 119, 261
- Chambers, J. E. 1999, Monthly Notices of the Royal Astronomical Society, 304, 793, doi: [10.1046/j.1365-8711.1999.02379.x](https://doi.org/10.1046/j.1365-8711.1999.02379.x)
- Chirikov, B. V. 1979, Physics reports, 52, 263
- Cincotta, P. M., Giordano, C. M., & Simó, C. 2003, Physica D Nonlinear Phenomena, 182, 151, doi: [10.1016/S0167-2789\(03\)00103-9](https://doi.org/10.1016/S0167-2789(03)00103-9)
- Cranmer, M., Tamayo, D., Rein, H., et al. 2021, arXiv preprint arXiv:2101.04117
- Dawson, R. I., Lee, E. J., & Chiang, E. 2016, The Astrophysical Journal, 822, 54
- Goldreich, P., Lithwick, Y., & Sari, R. 2004, Annu. Rev. Astron. Astrophys., 42, 549
- Goldreich, P., & Tremaine, S. 1979, Astronomical Journal, 84, 1638–1641, doi: [10.1086/112587](https://doi.org/10.1086/112587)
- . 1981, Astrophysical Journal, 243, 1062
- Gott III, J. R. 1993, Nature, 363, 315
- Gratia, P., & Lissauer, J. J. 2021, Icarus, 358, 114038
- Greenberg, R., & Van Laerhoven, C. 2011, The Astrophysical Journal, 733, 8
- Hadden, S. 2019, The Astronomical Journal, 158, 238

- Hadden, S., & Lithwick, Y. 2018, *The Astronomical Journal*, 156, 95
- Hadden, S., & Tamayo, D. 2022, *The Astronomical Journal*, 164, 179
- Hansen, B. M., & Murray, N. 2012, *The Astrophysical Journal*, 751, 158
- . 2013, *The Astrophysical Journal*, 775, 53
- Hénon, M. 1965, *Annales d'Astrophysique*, Vol. 28, p. 499, 28, 499
- Hénon, M., & Petit, J.-M. 1986, *Celestial Mechanics*, 38, 67
- Hoang, N. H., Mogavero, F., & Laskar, J. 2021, *Astronomy & Astrophysics*, 654, A156
- Hussain, N., & Tamayo, D. 2019, *Monthly Notices of the Royal Astronomical Society*, 491, 5258, doi: [10.1093/mnras/stz3402](https://doi.org/10.1093/mnras/stz3402)
- Kolmogorov, A. N. 1954, *Dokl. Akad. Nauk SSSR*, 98, 527. <https://cds.cern.ch/record/430016>
- Lammers, C., & Winn, J. N. 2024, arXiv preprint arXiv:2405.04527
- Laskar, J. 1989, *Nature*, 338, 237
- . 1990, *Icarus*, 88, 266
- . 2014, arXiv preprint arXiv:1411.4930
- Laskar, J., Fienga, A., Gastineau, M., & Manche, H. 2011, *Astronomy & Astrophysics*, 532, A89, doi: [10.1051/0004-6361/201116836](https://doi.org/10.1051/0004-6361/201116836)
- Lee, M. H., & Peale, S. J. 2002, *The Astrophysical Journal*, 567, 596
- Lichtenberg, A. J., & Lieberman, M. A. 2013, *Regular and chaotic dynamics*, Vol. 38 (Springer Science & Business Media)
- Lissauer, J. J., & Gavino, S. 2021, *Icarus*, 364, 114470
- Marzari, F., & Weidenschilling, S. 2002, *Icarus*, 156, 570
- Mogavero, F., & Laskar, J. 2021, *Astronomy & Astrophysics*, 655, A1
- Moser, J. 1973, *Stable and Random Motions in Dynamical Systems: With Special Emphasis on Celestial Mechanics* (Princeton University Press). <http://www.jstor.org/stable/j.ctt1bd6kg5>
- Murray, C. D., & Dermott, S. F. 2000, *Secular Perturbations* (Cambridge University Press), 274–320, doi: [10.1017/CBO9781139174817.008](https://doi.org/10.1017/CBO9781139174817.008)

- Namouni, F., Luciani, J.-F., Tabachnik, S., & Pellat, R. 1996, *Astronomy and Astrophysics*, v. 313, p. 979-992, 313, 979
- Obertas, A., Van Laerhoven, C., & Tamayo, D. 2017, *Icarus*, 293, 52
- Petit, A. C., Pichierri, G., Davies, M. B., & Johansen, A. 2020, *Astronomy & Astrophysics*, 641, A176
- Petrovich, C., Deibert, E., & Wu, Y. 2019, *The Astronomical Journal*, 157, 180
- Poincaré, H. 1899, *Les méthodes nouvelles de la mécanique céleste*, doi: 10.3931/e-rara-421
- Pu, B., & Wu, Y. 2015, *The Astrophysical Journal*, 807, 44
- Quarles, B., Quintana, E. V., Lopez, E., Schlieder, J. E., & Barclay, T. 2017, *The Astrophysical Journal Letters*, 842, L5
- Quillen, A. C. 2011, *Monthly Notices of the Royal Astronomical Society*, 418, 1043
- Quillen, A. C., & Faber, P. 2006, *Monthly Notices of the Royal Astronomical Society*, 373, 1245
- Rath, J., Hadden, S., & Lithwick, Y. 2022, *The Astrophysical Journal*, 932, 61, doi: 10.3847/1538-4357/ac5f57
- Rein, H., & Tamayo, D. 2015, *Monthly Notices of the Royal Astronomical Society*, 452, 376, doi: 10.1093/mnras/stv1257
- Ribas, Á., Bouy, H., & Merín, B. 2015, *Astronomy & Astrophysics*, 576, A52
- Smith, A. W., & Lissauer, J. J. 2009, *Icarus*, 201, 381
- Tamayo, D., Gilbertson, C., & Foreman-Mackey, D. 2021a, *Monthly Notices of the Royal Astronomical Society*, 501, 4798
- Tamayo, D., Murray, N., Tremaine, S., & Winn, J. 2021b, *The Astronomical Journal*, 162, 220, doi: 10.3847/1538-3881/ac1c6a
- Tamayo, D., Rein, H., Petrovich, C., & Murray, N. 2017, *The Astrophysical Journal Letters*, 840, L19
- Tamayo, D., Silburt, A., Valencia, D., et al. 2016, *The Astrophysical Journal Letters*, 832, L22
- Tamayo, D., Cranmer, M., Hadden, S., et al. 2020, *Proceedings of the National Academy of Sciences*, 117, 18194
- Tremaine, S. 2015, *The Astrophysical Journal*, 807, 157

- Van Laerhoven, C., & Greenberg, R. 2012, Celestial Mechanics and Dynamical Astronomy, 113, 215
- Volk, K., & Gladman, B. 2015, The Astrophysical Journal Letters, 806, L26
- Wang, J. J., Graham, J. R., Dawson, R., et al. 2018, The Astronomical Journal, 156, 192
- Weiss, L. M., Marcy, G. W., Petigura, E. A., et al. 2018, The Astronomical Journal, 155, 48
- Wisdom, J. 1980, Astronomical Journal, vol. 85, Aug. 1980, p. 1122-1133., 85, 1122
- Wisdom, J., & Holman, M. 1991, The Astrophysical Journal, 102, 1528, doi: [10.1086/115978](https://doi.org/10.1086/115978)
- Yang, Q., & Tamayo, D. 2023, arXiv e-prints, arXiv:2312.10031, doi: [10.48550/arXiv.2312.10031](https://doi.org/10.48550/arXiv.2312.10031)
- Zhang, K., Hamilton, D. P., & Matsumura, S. 2013, The Astrophysical Journal, 778, 6
- Zhu, W., Petrovich, C., Wu, Y., Dong, S., & Xie, J. 2018, The Astrophysical Journal, 860, 101